Dynamic surface reconstruction of perovskite oxides in oxygen evolution reaction and its impacts on catalysis: a critical review

Zhonghui Hu, Qian Yan, Yuanqing Wang*

Materials Genome Institute, Shanghai University, China

Corresponding author: yuanqingwang@shu.edu.cn

Abstract

Perovskite oxides have gained significant attention in recent years due to their superior catalytic activity in the oxygen evolution reaction (OER). However, the identification of the active structure and corresponding catalytic mechanism for these oxides still remains elusive, particularly for complex perovskite oxides. This is due to the intricate surface reconstruction that may occur under working conditions and the differing reaction mechanisms. This paper aims to address these issues by providing an overview of OER, perovskite oxides, characterization methods, and factors affecting surface reconstruction during OER. Specifically, the paper reviews in-situ and operando characterization studies conducted over the last decade, focusing on the surface dynamic structural evolution of simple and complex perovskite oxides such as $SrIrO_3$ and $Ba_{0.5}Sr_{0.5}Co_{0.8}Fe_{0.2}O_{3-\delta}$ (BSCF). The paper concludes by presenting an overview of reported active structures on perovskite oxides so far, and providing guiding principles for the design of highly active and stable catalysts. By addressing these issues, this paper provides valuable insights into the design and development of effective catalysts for OER.

Keywords: oxygen evolution reaction; perovskite oxides; surface reconstruction; operando characterization; active structures

Dynamic surface reconstruction

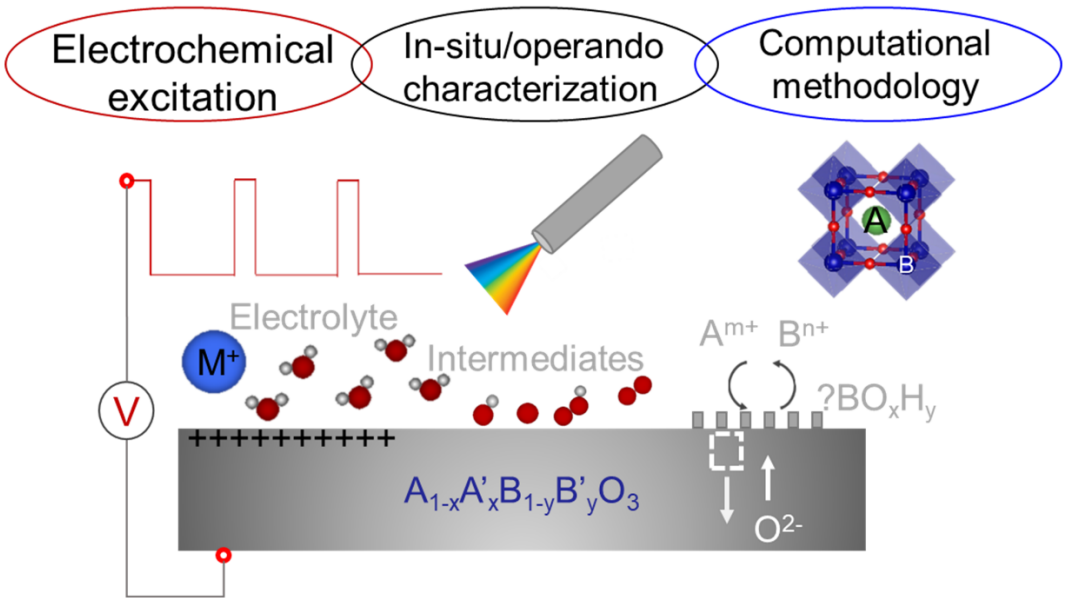

1. Introduction

The excessive use of fossil fuels, rapidly increasing energy demands, and severe environmental concerns have stimulated a pressing need to develop energy conversion systems that are cost-effective, efficient, and environmentally friendly[1]. Hydrogen, with its high energy density (120-142 MJ/kg) and clean reaction products (H_2O), is a promising energy carrier. It has the potential to not only alleviate current energy shortages in a sustainable manner but also to promote environmental restoration and economic growth[2]. As a result, hydrogen is increasingly being recognized as a key component of future energy systems. However, there is no abundant and pure source of hydrogen on Earth. Therefore, it is necessary to generate hydrogen from alternative sources, such as natural gas, coal, oil, water, and biomass[3].

Water electrolysis for hydrogen production offers numerous benefits. The reaction is thermodynamically spontaneous at a voltage of only 1.23 V (ΔG = 237.1 kJ/mol) under standard conditions, and sustainable energy sources like wind, hydroelectric, and nuclear power can provide the necessary electricity[4]. The process involves the hydrogen evolution reaction (HER) at the cathode and the OER at the anode, with the cathode requiring a two-proton-electron transfer process and the anode needing a four-proton-electron transfer process[5]. However, the kinetics of the OER are sluggish, prompting substantial research into finding efficient OER catalysts over the last few decades. Interested readers can refer to the comprehensive reviews on OER catalysts, such as those listed in references[6-16]. It's worth noting that IrO_2 and RuO_2 noble metal oxides still remain the most active OER catalysts, often used as benchmark catalysts to compare new ones.

Perovskite oxides have emerged as a promising family of non-noble metal oxides for catalyzing the OER[17-19]. In 2012, Shao-Horn's research group reported an exceptional OER activity of a perovskite oxide BSCF[20]. Its intrinsic OER activity was at least ten times higher than that of IrO_2 nanoparticles (average diameter ~6 nm). Subsequently, they discovered that perovskite oxides undergo surface reconstruction accompanied by the dissolution of metal ions

and improved catalytic activity under electrochemical conditions[21, 22]. This suggests a correlation between the dynamic surface structural evolution of the catalyst under working conditions and its activity. During the process of 'surface reconstruction', the catalyst undergoes changes in its composition, phases, and structures in response to external triggers, resulting in a variation in its catalytic performance. The external triggers during the OER process include operational conditions such as electrolyte pH, applied potential, cation of electrolyte, and more[23]. Surface reconstruction ultimately modulates the intrinsic properties of electrocatalysts, such as adsorption, activation, and desorption of intermediates, which can lead to reversible or irreversible alterations in the surface structure and performance[24-27]. The complexity of dynamic structural evolution under OER limits the application of ex-situ characterization techniques[28-30]. Hence, using in-situ and operando analytical techniques to observe the surface reconstruction phenomenon of OER electrocatalysts and track the real active structure is crucial for designing next-generation catalysts and clarifying the catalytic mechanism[31-33].

The purpose of this review is to examine the impacts of internal composition and external triggers on the restructuring of perovskite oxides under OER, and how this affects catalysis. While we will not provide a comprehensive overview of surface reconstruction phenomenon, we will focus on the examples of $SrIrO_3$, BSCF, and other related perovskite oxides over the past decade. In section 2, we will briefly introduce the OER mechanism, including the conventional adsorbate evolution mechanism (AEM) and lattice oxygen mechanism (LOM). Section 3 will summarize the properties of perovskite oxides and their applications in catalyzing OER. We will then highlight the importance of operando measurements in section 4, as we discuss the various characterization tools available for OER. In section 5, we will review the effects of inherent compositions and external triggers of surface reconstruction. Finally, we will summarize proposed active structures in the literature. We will conclude with the limitations of characterization methods on the OER mechanism in this field and an outlook

on potential future directions.

2. Mechanism of OER

Currently, there exist two primary formulations of the OER reaction mechanism: AEM[34, 35] and LOM[36, 37]. Fig. 1 (a) depicts the traditional AEM, which comprises four proton-electron transfer processes with metal serving as the active site[14, 38, 39]. The oxygen product is derived from absorbed water molecules. Initially, a water molecule is adsorbed on the metal site (M) of the electrocatalyst through a one-electron oxidation step, wherein it loses a proton simultaneously to form adsorbed *OH. The adsorbed *OH species is then oxidized, transferring one proton and electron, to *O. Another water molecule subsequently conducts a nucleophilic attack on the oxygen species to produce the *OOH intermediate. Finally, the *OOH adsorbed on the metal site is further oxidized, followed by desorption to release a dioxygen molecule. In contrast, LOM (depicted in Fig. 1 (b)) involves lattice oxygen of the catalysts in the oxygen evolution process and directly engages in O-O coupling[37, 39, 40]. The LOM pathway provides a unique reaction pathway for O-O coupling, and its reaction energy is not limited by the adsorption energy scaling relationship of the AEM pathway as will be discussed later.

The AEM reaction scheme under acidic condition comprises four elementary steps, as outlined below,

$$H_2O + * \rightarrow *OH + H^+ + e^- \quad (1)$$

$$*OH \rightarrow *O + H^+ + e^- \quad (2)$$

$$*O + H_2O \rightarrow *OOH + H^+ + e^- \quad (3)$$

$$*OOH \rightarrow O_2 + * + H^+ + e^- \quad (4)$$

The reaction free energy change under electrode potential can be calculated and formulated within the theoretical framework of computational hydrogen electrode (CHE) model[41]. More importantly, the free energy of a proton-electron pair can be equal to 1/2 H_2 in the gas phase at standard conditions plus -*e*U, where U is the electrode potential with respect to the reversible hydrogen electrode (RHE) which is widely used by experimentalists. And the potential is reported with respect to RHE scale in the

whole review unless otherwise stated. Using this framework, the Gibbs free energy change of each step at standard conditions (pH = 0, T = 298.15 K) can be written as follows by defining the adsorption free energy of intermediates (e.g., *OH) with respect to H_2O and H_2[34, 35, 42, 43]:

$$\Delta G_1(U) = \Delta G_{*OH} - eU \quad (5)$$

$$\Delta G_2(U) = \Delta G_{*O} - \Delta G_{*OH} - eU \quad (6)$$

$$\Delta G_3(U) = \Delta G_{*OOH} - \Delta G_{*O} - eU \quad (7)$$

$$\Delta G_4(U) = \Delta G_{O2} - \Delta G_{*OOH} - eU \quad (8)$$

where ΔG_{*X} represents adsorption free energy of a reaction intermediate *X and ΔG_{O2} represents free energy of an oxygen molecule in terms of the H_2O and H_2 energetics and equals 4.92 eV. Further analysis shows that the adsorption free energies on metal oxides are inter-connected by a so called 'scaling relationship'[35, 43]:

$$\Delta G_{*OH} \approx 0.61\Delta G_{O*} - 0.58\ eV \quad (9)$$

$$\Delta G_{*OOH} \approx 0.64\Delta G_{O*} + 2.40\ eV \quad (10)$$

By substituting the expression of Gibbs free energy changes with Eqs. 9 and 10, we obtain:

$$\Delta G_1(U) \approx 0.61\Delta G_{*O} - 0.58\ eV - eU \quad (11)$$

$$\Delta G_2(U) \approx 0.39\Delta G_{*O} + 0.58\ eV - eU \quad (12)$$

$$\Delta G_3(U) \approx -0.36\Delta G_{*O} + 2.40\ eV - eU \quad (13)$$

$$\Delta G_4(U) \approx -0.64\Delta G_{*O} + 2.52\ eV - eU \quad (14)$$

A thermodynamic limiting potential (U_L) in each step can be defined as the least potential applied to make the reaction free energy change negative by setting Eqs. 11-14 zero:

$$U_{L1} = (0.61\Delta G_{*O} - 0.58\ eV)/e \quad (15)$$

$$U_{L2} = (0.39\Delta G_{*O} + 0.58\ eV)/e \quad (16)$$

$$U_{L3} = (-0.36\Delta G_{*O} + 2.40\ eV)/e \quad (17)$$

$$U_{L4} = (-0.64\Delta G_{*O} + 2.52\ eV)/e \quad (18)$$

It is immediately seen that the step with the largest value of U_L dictates the overall reaction thermodynamically since this specific applied U_L would make the overall energy diagram downhill, which is thus called 'potential determining step' (PDS). By

plotting U_L as a function of ΔG_{*O}, a "volcano" shape plot can be constituted by solid thick blue and green lines as shown in Fig. 1 (c)[35, 43]. On the left leg of volcano, strong *O binding side, the overall limiting potential is controlled by the energetics of step 3 (PDS in this case). While on the right side of volcano, weak *O binding side, the overall limiting potential is controlled by step 2. The optimal catalyst should be the one locating at the top of volcano plot with a proper adsorption free energy of ΔG_{*O}, which is analogous to the famous Sabatier Principle[44]. It can be also envisioned from Fig. 1 (d) that even the optimal catalyst has a non-zero overpotential due to the restriction of scaling relationships. And this overpotential is called the theoretical overpotential (η_{theo}). It is defined as:

$$\eta_{theo} = max\{U_{L1}, U_{L2}, U_{L3}, U_{L4}\} - 1.23\ V = max\{\ U_{L2}, U_{L3}\} - 1.23\ V \quad (19)$$

since we are only interested in the region near the top which is dictated by either the energetics of step 2 or step 3. By closely checking Eqs. 9 and 10, one may find that there is approximately a constant difference of $\Delta G_{*OOH} - \Delta G_{*OH}$ which equals around 3.2 eV. For this reason, Eq. 19 can be rewritten as

$$\eta_{theo} = max\{\ U_{L2}, U_{L3}\} - 1.23\ V = \max\{\frac{\Delta G_{*O} - \Delta G_{*OH}}{e}, \frac{\Delta G_{*OOH} - \Delta G_{*O}}{e})\} - 1.23\ V =$$

$$\max\{\frac{\Delta G_{*O} - \Delta G_{*OH}}{e}, \frac{3.2\ eV - (\Delta G_{*O} - \Delta G_{*OH})}{e}\} - 1.23\ V \quad (20)$$

As can be seen from Eq. 20, the minimum theoretical overpotential is 370 mV when $\Delta G_{*O} - \Delta G_{*OH} = 1.60\ eV$.

Several points and assumptions must be addressed regarding this topic. Firstly, it has been commonly assumed that each elementary step involves concerted proton-electron transfer (CPET) [45, 46]. However, recent studies have shown that it is possible to decouple or tune the proton-electron transfer[46, 47], as seen in the identification of a key intermediate $NiOO^-$ from deprotonation and the subsequent discovery of this decoupled proton-electron transfer mode in perovskite[36]. Secondly, the active site throughout this mechanism has been assumed to be a single metal site due to the kinetically hindered direct recombination of oxygen atoms on a dual-metal site through theoretical calcualtions[48], although some theoretical studies suggest a dual-metal site involved OER mechanism[49, 50]. Recently, a spin transition mechanism was

suggested to overcome the high activation barrier on a dual-iridium site model, supported by DFT calculation and in-situ ultraviolet–visible (UV-Vis) spectroscopy[51]. Thirdly, the predicted minimum value of the theoretical overpotential according to the AEM mechanism is 370 mV, which is not fully consistent with some experimental results (η << 370 mV)[15, 52]. This discrepancy has prompted theoretical and experimental scientists to seek new explanations.

The study of the LOM mechanism can be traced back to the study of PtO catalysts reported by Damjanovic and Jovanovic in 1976[53], who suggested that oxygen atoms in the surface oxide films is involved in the OER. Bockris further proposed the involvement of lattice oxygen on perovskites[18, 19]. With the advent of differential electrochemical mass spectroscopy (DEMS) combined with isotope labelling experiment, the participation of lattice oxygen in the product has been identified in RuO_2[54, 55], IrO_2[56, 57] and perovskite oxides[36, 58]. In contrast to these studies, Stoerzinger et al. reported that there is no lattice oxygen exchange during the OER on the surfaces of RuO_2 (100), (110), (101), and (111) regardless of the pH of the electrolyte[59]. Additionally, Scott et al. concluded that the lattice oxygen evolution mechanism into O_2 is not the dominating oxygen evolution mechanism (negligible contribution) on Ru- and Ir-based oxides in acidic medium with the aid of a highly sensitive electrochemistry - mass spectrometry (EC-MS) setup[60]. They highlighted the importance of distinguishing between labelled oxygen evolution and lattice oxygen mediated catalytic mechanisms when conducting isotopic OER experiments.

In perovskite oxide, Mefford et al. discovered a correlation between the oxygen vacancy concentration and oxygen diffusion coefficient of $La_{1-x}Sr_xCoO_{3-\delta}$ and the corresponding catalytic activity which follows their hypothesis on the role of lattice oxygen on $LaNiO_3$[61-63]. The study found that an increase in oxygen vacancy or oxygen diffusion coefficient led to a linear increase in OER activity. Through DFT calculations, they identified a key intermediate with adsorbed –OO and lattice O vacancy that determines the LOM over AEM by its relative stability to conventional adsorbed –O intermediate[61, 64]. They also linked the stability of the catalyst to the

reaction mechanism, suggesting that catalysts with low stability tend to follow the LOM reaction mechanism. Later, Binninger et al. speculated that the ABO_3 perovskite oxide would dissolve A and B cations into the electrolyte under OER via LOM based on thermodynamics in which B cation would redeposite with OH^- forming a hydrous amorphous layer[65]. As shown in Fig.1 (e), Kolpak group found that for strongly bound lanthanide perovskite oxides, the OER process following the LOM mechanism is thermodynamically limited by $OH^* \rightarrow V_O + OO^*$ (V_O for oxygen vacancy, black line in Fig. 1 (e)), whereas for moderately bound perovskite oxides, limited by $V_O + OO^* \rightarrow V_O + O_2(g) + OH^*$ (red line in Fig. 1 (e)), while for weakly bound perovskite oxides, limited by $H_{O\text{-}site}^* + OH^* \rightarrow OH^*$ (green line in Fig. 1 (e))[37]. The theoretical minimum overpotential is estimated to be 0.17−0.41 eV for LOM depending on whether the red line is included in the volcano plot or not due to concern of DFT calculation uncertainty. Shao Horn and Koper's research group subsequently confirmed that the O_2 generated on some perovskite contains lattice oxygen from oxides by isotope labeling and in-situ mass spectrometry[36]. Slightly different from aforementioned LOM, lattice oxygen was proposed to react with adsorbed oxygen to form an O_{ads}-O_{latt} bond which acts as an active site, and then dioxygen is released through non-concerted proton-electron transfer as evidenced from the pH-dependent OER activity on the RHE scale (Fig. 1 (c)).

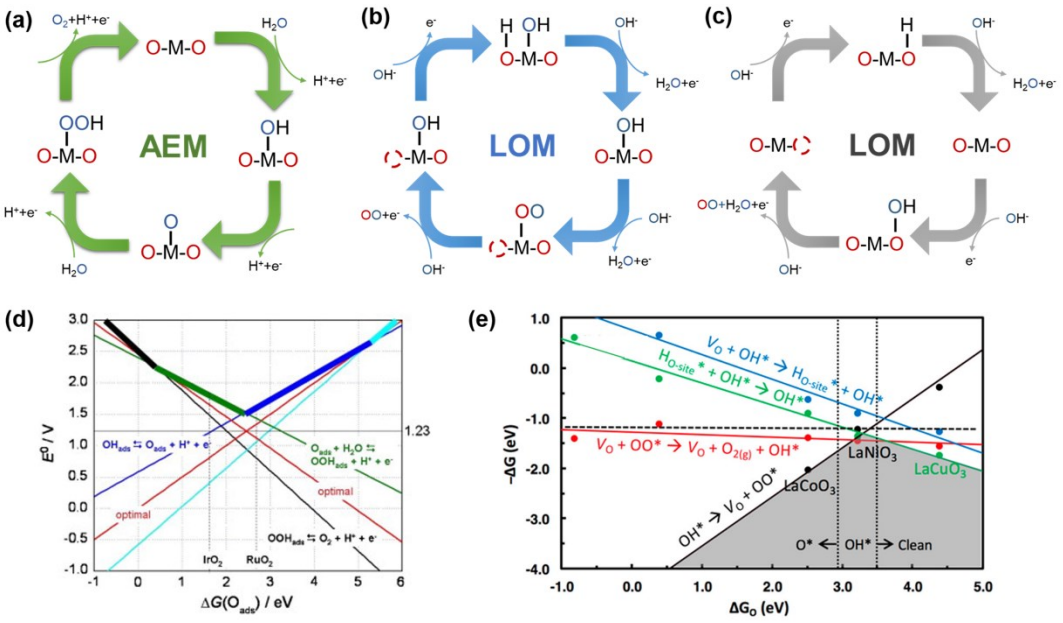

Figure 1. Schematic illustration of the proposed traditional AEM (a) and two LOMs (b-c) for OER mechanism. Equilibrium potentials or negative reaction free energies as a function of the adsorption free energy of oxygen on metal oxides based on AEM[43] (d) and LOM[37] (e), respectively. (d) Reproduced with permission[43]. Copyright 2011, Elsevier. (e) Reproduced with permission[37]. Copyright 2018, American Chemical Society

3. Perovskite oxides

Effective OER catalysts conventionally were made of precious metals such as ruthenium or iridium oxides. However, due to the limited reserves of these materials, they are remarkably expensive. For this reason, there is a need to develop low-cost OER catalysts that exhibit high activity and stability in order to move towards a carbon-neutral society. Recently, perovskite oxides have gained attention. These materials were originally discovered by Gustav Rose, a German mineralogist, in 1839. They have a chemical formula of $CaTiO_3$ and were named after Lev Perovski, a Russian mineralogist (1792-1856)[66]. Perovskite oxides are attractive due to their abundant elemental composition, good catalytic activity, and low cost, which have fueled intensive research in the catalysis field[67].

The perovskite oxide has a molecular formula of ABO_3, where A cation is in 12-fold coordination and B cation is in 6-fold coordination as shown in Fig. 2 (a) in its ideal cubic phase[68, 69]. This oxide offers an extensive chemical space due to its structural variation and component flexibility. The

three primary distortion mechanisms, including octahedral distortion, B-site displacement, and octahedral tilting, lead to the formation of various crystal structures such as tetragonal, orthorhombic, hexagonal, monoclinic, and triclinic phases[70]. One of the key descriptors used to characterize the formation of perovskite oxide is called tolerance factor *t*, which is calculated using the following equation,

$$t = \frac{(r_A + r_X)}{\sqrt{2}(r_B + r_X)} \quad (21)$$

where r_A, r_B, r_X are the ionic radii of the cation A, cation B and anion X. In 1926, Goldschmidt proposed a method to predict which crystal structure is preferred based on the tolerance factor[71]. If the tolerance factor falls between 0.9 and 1, the crystal structure is cubic, while lower values between 0.71 and 0.9 result in a rhombohedral or orthorhombic phase. A tolerance factor between 1 and 1.13 favors a hexagonal or tetragonal structure, and non-perovskite structures form when the tolerance factor exceeds 1.13 or falls below 0.71[72]. Recently, a new tolerance factor, denoted as τ, has been proposed using a SISSO (sure independence screening and sparsifying operator) based approach, which has been shown to correctly predict the crystal structure of 92% of compounds as either perovskite or nonperovskite [73]. It has the following form,

$$\tau = \frac{r_X}{r_B} - n_A\left(n_A - \frac{r_A/r_B}{\ln(r_A/r_B)}\right) \quad (22)$$

where n_A is the oxidation state of element A.

In total, 2346 types of ABO_3 perovskites can be formed when different metals occupy the A and B sites. The A site cation can be an alkali metal element, an alkaline earth metal element, or a rare-earth metal element, while the B site cation is mainly a transition metal element[74, 75]. The A or B site can also contain two different cations, forming a double perovskite oxide $A'A''B_2O_6$ or $A_2B'B''O_6$. More complex perovskites represented by $A'_xA''_{1-x}$ $B'_yB''_{1-y}O_6$ are possible through cation mixing. In addition, oxygen deficiency is quite common in preparing perovskite oxides further

leading to the increase of complexity, such as BSCF[20], $SrCo_{0.8}Fe_{0.2}O_{3-\delta}$[22], $La_{1-x}Sr_xCoO_{3-\delta}$[61], and $SrNb_{0.1}Co_{0.7}Fe_{0.2}O_{3-\delta}$[76]. Ordering of these oxygen vacancies in extreme cases leads to the so called "brownmillerite" ($A_2M_2O_5$) structure formation[77]. The presence of oxygen vacancies was proved to affect the OER activity via tuning the value of oxygen deficiency δ [78].

Several methods can be used to synthesize perovskite oxides, including the solvothermal[79], sol-gel[80], Pechini[81], co-precipitation[20], combustion[20, 82], solid-state reaction[83], and pulse laser deposition methods[84]. Among these, the sol-gel method is frequently used, where metal salts are dissolved in deionized water, chelating agents are added, and the pH of the solution is adjusted to be weak alkaline before heating to form a viscous gel. The gel is then heated and calcined at high temperature under certain atmosphere to obtain the perovskite oxide. The calcination temperature and atmosphere (inert or partial pressure of oxygen) are critical in forming the perovskites[85-87]. In particular, thin film material can be obtained through pulse laser deposition. The thickness of film can be controlled by varying the counts of laser pulses. The usage of thin film catalyst is especially useful for studying the surface properties which is directly related to catalysis.

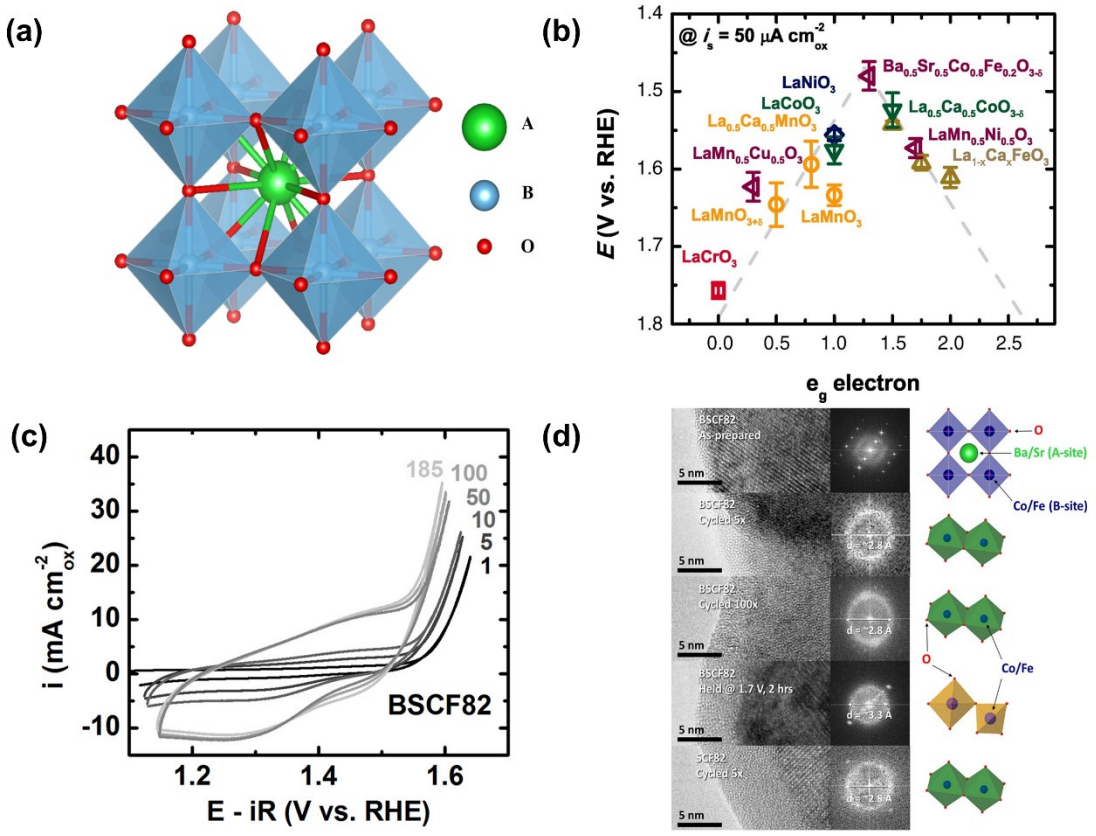

Figure 2. (a) Representation of perovskite oxide crystal structure. (b) The volcano plot of OER activity of perovskites (overpotentials achieved at 50 μA·cm_{ox}^{-2}) as a function of e_g orbital filling[20]. (c) Cyclic voltammograms (10 mV/s) of BSCF in oxygen-saturated 0.1 M KOH electrolyte[21]. (d) High-resolution transmission electron microscopy (HRTEM) images and corresponding fast Fourier transforms (FFT) of particle surfaces collected from BSCF as-prepared powder, BSCF electrodes after distinct electrochemical treatments and $SrCo_{0.8}Fe_{0.2}O_{3-\delta}$ electrode after 5 cycles. The corresponding structural variations are shown in the right side[21]. (b) Reproduced with permission[20]. Copyright 2011, the American Association for the Advancement of Science. (c-d) Reproduced with permission[21]. Copyright 2012, American Chemical Society.

In the 1970s, Meadowcroft pioneered the application of perovskite oxides as oxygen electrode materials and identified $LaCoO_3$ as a promising oxygen electrocatalyst[17]. The development of perovskite oxides in OER was accompanied by the discovery of new descriptor. In 1980, Matsumoto et al. studied $La_{1-x}Sr_xFe_{1-y}Co_yO_3$ series oxides applied in alkaline electrolyte and found that the OER activity is affected by the σ^* band of the oxide and the oxidation state of transition metal[88]. Later in 1983 and 1984, Bockris et al. systematically studied the correlation of catalytic activity with the electronic structure of perovskites[18, 19]. In a serials of studied perovskite oxides (B site cation is V, Cr, Mn, Fe, Co and Ni), the current density from

$LaNiO_3$ is the highest, much higher than $LaCoO_3$. Furthermore, the occupancy of antibonding orbitals of M^z-OH (M is B site cation) determines the electrocatalytic activity.

In 2002, Bursell et al. studied the catalytic activity of $LaNiO_3$, $La_{0.1}Ca_{0.9}MnO_3$ and $La_{0.6}Ca_{0.4}CoO_3$ in alkaline electrolytes for OER and ORR[89]. Then, in 2011, Yang Shao-Horn group reported a perovskite oxide $Ba_{0.5}Sr_{0.5}Co_{0.8}Fe_{0.2}O_{3-\delta}$ that achieved significantly high activity with an overpotential of around 250 mV @ 50 μA/cm^2, at least an order of magnitude higher than the benchmark iridium oxide catalyst[20]. The authors proposed that the specific OER activity of perovskite oxides exhibits a volcano shape dictated by the e_g orbital filling of surface B-site cations. For single perovskite oxides such as $LaNiO_3$ and $LaCoO_3$, which are located near the top of the volcano, they have better OER activity. For complex perovskite oxides such as BSCF, which is almost at the top of the volcano ($e_g \approx 1.2$, $t_{2g}^5 e_g^{1.2}$), it has the highest OER activity among the oxides studied. This report has stimulated a new wave of studying perovskites in OER, and some new catalysts have been synthesized with the guidance of the new descriptor. For instance, Kim et al. synthesized an oxygen-deficient perovskite $Ca_2Mn_2O_5$ by using hydrogen as a reducing agent, which can catalyze the oxygen evolution current at around 1.50 V[90]. The reduction treatment makes the electronic configuration of manganese from Mn^{4+} ($t_{2g}^3 e_g^0$) in $CaMnO_3$ to Mn^{3+} ($t_{2g}^3 e_g^1$) in $Ca_2Mn_2O_5$. The presence of Mn^{3+} facilitates the interaction of e_g orbital with O-p_σ orbital of OH^- resulting in moderate bonding strength and faster OER kinetics. A similar approach of regulating spin state was achieved in $LaCoO_3$ by preparing a thin film on differently oriented $LaAlO_3$ substrates[91]. The Co^{3+} optimal spin state ($t_{2g}^5 e_g^{0.87}$) grown on the (100) substrate exhibits superior activity compared to those grown on the (110) and (111) substrates, with estimated e_g orbital fillings of 0.48 and 0.31, respectively.

In 2013, Yang Shao-Horn's group discovered a new class of double perovskites, namely $(Ln_{0.5}Ba_{0.5})CoO_{3-\delta}$ (Ln = Pr， Sm, Gd and Ho), that exhibit comparable activity to BSCF[92]. Along with these findings, a new descriptor known as the O *p*-band center relative to the Fermi level of the perovskite was proposed, showing a linear relationship with the OER activity. As the identification of LOM in perovskite oxides emerged,

attention was given to the role of lattice oxygen, which can also function as an active site[36]. Therefore, the covalency of the metal-oxygen bond was recognized as a crucial property when the e_g orbital filling of the transition metal established on the ionic model, which assumes only the metal site as the active site, ignores the sharing of electrons. The O *p*-band center relative to the Fermi level can be used to quantify the covalency of the metal-oxygen bond, which was later extended to a new descriptor called "charge transfer energy" (energy difference between the unoccupied metal *3d*- and occupied O *2p*-band centers) [16, 93, 94]. Yamada et al. prepared a series of perovskite oxides ABO_3 (A=Ca, Sr, Y, La; B=Ti, V, Cr, Mn, Fe, Co, Ni, Cu) and confirmed that the charge transfer energy is the most appropriate descriptor among the descriptors proposed by correlating experimental activity data with calculated descriptor values based on DFT calculations[95].

While many perovskite oxides have shown high catalytic performance and new descriptors have been developed, some reports have revealed that the surface structure of some perovskite oxides is actually not stable under OER conditions. For instance, the highly active BSCF was found to undergo a surface transformation during electrochemical conditions, as reported by the same group that discovered its activity in OER[20, 21]. They observed that as the number of cyclic voltammetry (CV) scans increased, the current density also gradually increased (Fig. 2 (c)). As illustrated in Fig. 2 (d), the transformation of the initial crystalline surface region of BSCF into an amorphous layer with a thickness of ~8 nm after five cycles was found, and the amorphous region increased with further cycles. This amorphizaition was also found in $SrCo_{0.8}Fe_{0.2}O_{3-\delta}$. The formation of edge-sharing Co/Fe octahedra on the surface of the cycled BSCF was also suggested by fast Fourier transform (FFT) analysis of high-resolution transmission electron microscopy (HRTEM) images, in contrast to the corner-shared octahedra present in the initial perovskite structure. Additionally, a spinel-like structural pattern with octahedral and tetrahedral Co/Fe cation coordination was indicated in the amorphized surface region of the BSCF electrode held at 1.7 V for 2 h[21, 96]. This surface reconstruction phenomenon with increased activity occurring on the surface of perovskite oxide during OER is crucial for identifying the real active

site of perovskite oxides. Therefore, in-situ and operando characterizations are needed to reveal this phenomenon. A brief introduction to characterization tools often used in electrocatalysis is given in the next section before reviewing the surface reconstruction literature under OER.

4. Characterization methods

This section provides an introduction of the most commonly used characterization tools in OER studies, including electron microscopy, X-ray-based techniques, and optical spectroscopy. Rather than delving into the principles of these techniques, we focus on their technical aspects and their specific applications in OER research. While ex-situ methods are useful, they cannot capture the dynamic structural changes and intermediate species during the reaction, highlighting the need for in-situ characterization methods[97]. Furthermore, to overcome the limitations of the "materials gap" and "pressure gap" in catalysis research, operando methodology has emerged as a powerful tool to directly correlate the dynamic structure of a catalyst with its performance under realistic conditions[98, 99]. Originally developed in the field of heterogeneous catalysis, operando techniques have been increasingly employed in OER research, and their recent applications are discussed in this section.

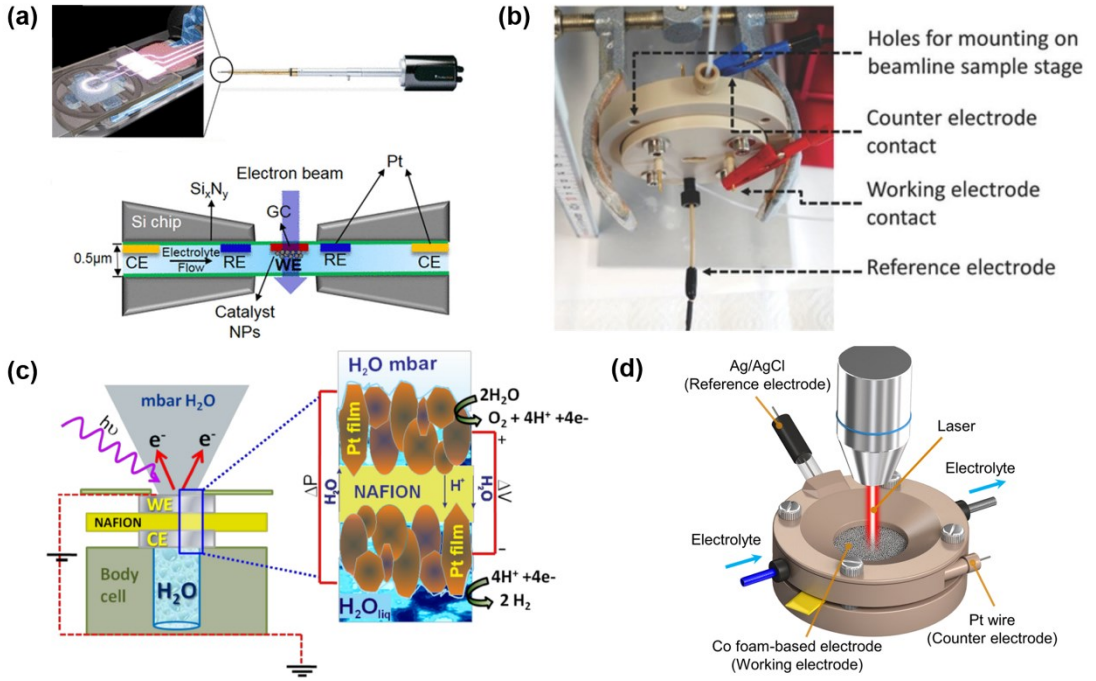

Figure 3. Schematic illustrations of in-situ/operando characterization tools. (a) In-situ electrochemical TEM holder: WE, CE, and RE are the working, counter, and pseudoreference electrodes, respectively[100]. (b) Electrochemical flow-cell setup for in-situ XAS[101]. (c) NAP-XPS[102]. (d) Raman spectroscopy[103]. (a) Reproduced with permission[100]. Copyright 2019, American Chemical Society. (b) Adapted under CC BY license from ref. [101]. (c) Adapted under CC BY license from ref. [102]. (d) Adapted under CC BY license from ref. [103].

4.1 Electrochemical methods

CV is a commonly used method for testing the activity of OER catalysts. By cycling the potential in a certain range and recording the current (activity) simultaneously, the structural changes of the catalyst may be observed as the number of CV scans increases as mentioned in section 3. The formation of redox peaks during CV would be related to the formation of active structures, which is typically observed in multi-valent metal oxides. For example, on an IrO_x electrode, a reversible peak at 0.9 V is attributed to the Ir^{3+}/Ir^{4+} redox couple prior to the water oxidation current, serving as a precursor for the formation of an Ir^{5+} species responsible for initiating oxygen evolution[51]. In the case of $La_{1-x}Ce_xNiO_3$ perovskites, the oxidation peak occurs at 1.42 V for $LaNiO_3$ and at a lower potential for the Ce-doped perovskites. This peak is related to the formation of the NiOOH active layer[33]. Note that the redox peak intensity is proportional to the square root of the scan rate assuming a reversible process.

For this reason, the oxidation of metal ions may not be noticeable at slow scan rates. By adopting rotating ring-disk electrode (RRDE), Faradaic efficiency is determined from the ring and disk currents and collection efficiency to distinguish OER current from side reactions[104].

Chronoamperometry (CA) and chronopotentiometry (CP) are commonly used techniques to evaluate catalyst stability. In CA, current density is measured over time at a constant potential, while in CP, potential variation is measured over a fixed current density. A study conducted by You et al.[105] investigated the stability of three-dimensional hierarchically porous urchin-like Ni_2P microspheres on nickel foam (Ni_2P/Ni/NF) using CP test fixed at 10 mA/cm^2. The results show a gradual increase in required potential at the beginning of the test (~6 h), which is partly attributed to the possible formation of active nickel oxides/hydroxides/(oxy)hydroxides formation, as evidenced by the smoothness of the chronopotentiometric curve in contrast to the noise of the curve when oxygen bubbles are observable.

By designing a pulse voltammetry protocol assisted by X-ray adsorption and X-ray diffraction methods, one can steer and analyze the ensemble of coexisting copper species on the copper electrode quantitatively correlating it with their performance on the selectivity of CO_2 reduction[106]. In addition, electrochemical impedance spectroscopy (EIS) can be used as a characterization tool in OER to identify relevant kinetic parameters. However, it is important to choose an appropriate electronic equivalent circuit and applied potential with care[107]. Several studies have utilized EIS to investigate OER activity and identify rate-determining steps[108, 109].

4.2 Transmission Electron Microscopy (TEM)

The TEM is capable of providing atomic-resolution microstructure images of materials due to the short wavelength of the electron beam. To obtain chemical information at the atomic level, TEM can be assisted by techniques such as energy-dispersive X-ray spectroscopy (EDS) and electron energy loss spectroscopy (EELS)[110]. It is important to note that a high vacuum is required for electrons to transmit coherently in traditional

TEM. However, the development of liquid cell TEM, in which a liquid medium is confined around the sample, enables the observation of physical changes in electrocatalysts in an in-situ TEM fashion[111].

Fig. 3 (a) illustrates the setup of an "electrochemical chip," which serves as the electrochemical cell and is located at the tip of a sample holder. Within the electrochemical chip, a three-electrode system is present, consisting of a working electrode made of glassy carbon and two Pt electrodes serving as the pseudoreference electrode and counter electrode, respectively. The particle material of interest is deposited on the glassy carbon electrode between two electron-transparent silicon nitride windows. The electrolyte flows through the electrochemical cell with a thickness of 0.5 µm.

Researchers, such as Ersen et al., have utilized this setup to study Co_3O_4 nanoparticles during the OER under operational conditions[100]. By combining techniques such as CV or chronopotentiometry with scanning transmission electron microscopy (STEM), they were able to directly observe the growth of amorphization of Co_3O_4 nanoparticles during the OER process. The amorphous regions, characterized by less dense contrast in STEM images, were attributed to the formation of a cobalt (oxy)hydroxide-like phase with an irreversible nature.

4.3 X-ray Absorption Spectroscopy (XAS)

XAS is a powerful technique used to investigate the electronic and geometric structure of catalysts[112]. By tuning the x-ray energy to excite the core level electrons of the absorbing atoms to unoccupied states, an absorption edge is induced in the absorption spectrum. The features observed near this edge are referred to as x-ray absorption near edge structure (XANES). XANES provides valuable information about the oxidation state and electronic structure of the absorbing atoms based on their characteristic core level energetics. Beyond the absorption edge, the

features are referred to as extended x-ray absorption fine structure (EXAFS), which extends to a few thousands of electron volts above the edge. EXAFS provides insights into the local environment of the absorber, including bonding lengths and coordination numbers, by analyzing the interference phenomenon between the outgoing photo-electron wave generated by x-ray absorption and the backscattered wave.

XAS signals can be collected using transmission mode, fluorescence, and total electron yield (TEY) modes. Monitoring the emission of Auger electrons, which is a secondary process of X-ray absorption, allows for the assessment of the absorption coefficient. Due to the short mean free path of Auger electrons, this measurement is particularly sensitive to the surface region (approximately 1-5 nm)[113, 114].

XAS is widely employed to study perovskite materials because of its element-specific nature, which is suitable for examining variations in the electronic structure of each element present in perovskites[115]. In order to study OER in an IrO_2-TiO_2 catalyst, a three-electrode cell design with flowing electrolyte for XAS experiments is presented in Fig. 3 (b)[101]. The electrochemical chamber consists of two Kapton foils serving as X-ray beam windows. The bottom Kapton foil can be coated with the studied material, acting as the working electrode, while the top Kapton foil serves as the counter electrode. The thin and flowing electrolyte enables measurements in both transmission and fluorescence modes and helps suppress the interference caused by bubble formation. In-situ XANES results reveal that above the OER onset potential (approximately 1.4 V), a continuous increase in the oxidation state of Ir is observed, as evidenced by the intensification of the white line peak near the absorption edge. Below the OER onset potential, a constant electronic structure of Ir is suggested. The EXAFS data aligns well with the rutile IrO_2 structure, indicating a distorted Ir-centered octahedron coordinating six oxygen atoms.

4.4 X-ray photoelectron spectroscopy (XPS)

X-ray photoelectron spectroscopy (XPS) is a widely used analytical tool for investigating the composition and electronic structure of solids. It relies on the measurement of emitted photoelectrons' kinetic energy to determine their binding energy, which is element-specific and provides information about the oxidation state of the elements involved[116]. XPS has advantages in terms of probing depth due to the short inelastic mean free path (IMFP) of photoelectrons in solids, which restricts the analysis to only a few nanometers[117]. This feature renders XPS particularly valuable for catalysis studies.

Conventional XPS requires an ultrahigh vacuum environment to minimize electron scattering in the gas phase. To address this issue, near ambient pressure XPS (NAP-XPS) was developed, allowing analysis at pressures in the torr range[118] or even several bars[119]. Fig. 3 (c) illustrates a typical setup for NAP-XPS[102] . It is shown that the liquid diffuses from the inner reservoir through the membrane, facilitated by the pressure difference between the reservoir and the evacuated measurement chamber, as well as the porosity of the working electrode (WE) and counter electrode (CE) films. This diffusion process opens the channels in the membrane, allowing the liquid to enter the measurement chamber. As a result, a water pressure in the millibar range is generated within the measurement chamber. In this setup, the electron analyzer remains in a high vacuum while being separated from the high-pressure sample chamber by a series of differentially pumped electrostatic lenses and apertures. This differential pumping approach minimizes the path of photoelectrons in the gas phase. By combining NAP-XPS with electrolysis reactions, it becomes possible to investigate the surfaces of materials such as Pt or Ir during the OER[120, 121]. For instance, when applying OER conditions to an Ir film, a mixed-valent $Ir^{III/IV}$ matrix was identified, while under open circuit potential, the main contribution was from metallic Ir.

Furthermore, by implementing a protective sample transfer procedure, quasi-in-situ XPS measurements can be easily conducted using a laboratory XPS

instrument[122] . By this technique, during OER in a 1 M KOH solution, surface restructuring into a cobalt hydroxide/oxide surface on CoP nanoparticles was observed. Over time, the Co-P feature in the Co 2p spectra disappeared, accompanied by the appearance of a Co-O feature. Additionally, the O 1s spectra revealed a significant OH component at 531.5 eV and a minor lattice oxygen (O-Co) feature at 530.0 eV after 30 seconds of OER.

4.5 Vibrational spectroscopy and other tools

Vibrational spectroscopy encompasses two primary characterization methods: infrared (IR) spectroscopy and Raman spectroscopy. These techniques serve as complementary tools for monitoring the vibrational properties of molecules or solids. Spectrum features are observed when there is a change in the dipole moment (IR spectroscopy) or polarizability (Raman spectroscopy) of the substrate during vibration.

There are several differences between these techniques in the context of OER characterization. Firstly, Raman scattering effect is very weak, requiring laser excitation to promote the detection. However, this can potentially lead to the well-known issue of "laser damage" to catalysts[123]. On the other hand, IR spectroscopy is relatively stronger in signal collection due to the absorption of light at specific frequencies corresponding to vibrations. Secondly, Raman spectroscopy is less sensitive to water molecules compared to IR spectroscopy. Therefore, Raman spectroscopy is more suitable for water-involved reactions if the region of interest for vibration overlaps with that of water. Thirdly, IR spectroscopy displays high sensitivity to certain molecules in the gas phase, such as CO_2. In contrast, Raman scattering typically has negligible contributions from gas-phase molecules[124].

Conventional IR and Raman spectroscopy are not inherently surface-sensitive techniques. However, it is possible to detect adsorbed species or probe the surface structure of solids by employing surface-enhanced

techniques, such as surface-enhanced infrared reflection absorption spectroscopy (SEIRAS)[125] and surface-enhanced Raman spectroscopy (SERS)[126].

SEIRAS was utilized to confirm the presence of superoxide anion (O_2^-) in the oxygen reduction reaction (ORR) on a Pt film electrode under alkaline conditions, where rapid protonation is inhibited (above the pKa 4.8 of $OOH\cdot/O_2^-$)[127]. The vibrational band corresponding to the superoxide species appears at 1005-1016 cm^{-1}, coinciding with the onset of ORR current at 0.2 V vs. Ag/AgCl. In acidic conditions, Kukunari et al. also reported the detection of superoxide species (O_2^-) at 1095 cm^{-1} using SEIRAS[128].

A typical setup for in-situ Raman spectroscopy is depicted in Fig. 3 (d)[129]. The laser is focused onto the electrode surface using an objective lens, which also collects the back-scattered light. The collected light is then directed to a monochromator and a photon counting system for spectral generation. In the context of OER, Yeo et al. utilized an in-situ Raman setup to observe the transformation of Co_3O_4 into CoO(OH) (503 cm^{-1}) and CoO_x species (579 cm^{-1}) on cobalt oxide films deposited on Au surfaces[130]. The Koper group employed a similar in-situ Raman spectroscopy approach to investigate a nickel-based catalyst deposited on a roughened Au electrode[46, 131]. They observed the in-situ formation of active oxygen species following the formation of γ-NiOOH (~479 and 562 cm^{-1}). These Raman peaks were attributed to a superoxo-type intermediate called 'NiOO', which is located in the 900-1150 cm^{-1} range.

There are several additional characterization methods that can be useful in studying OER. One example is vibrational sum frequency (VSF) spectroscopy, which is a surface-specific technique that can provide insights into the intermediates involved in OER[132]. Another valuable technique is UV-Vis spectroscopy, which is commonly used to characterize the redox transitions of transition metals, such as Ni^{2+}/Ni^{3+} redox transition in OER[131, 133].

5. Surface Reconstruction under working conditions

Advancements in structural characterization techniques have facilitated the exploration of surface reconstruction in a wide range of OER catalysts, including metal alloys, transition metal sulfides/selenides/nitrides/phosphides, and metal oxides[134-138]. This section aims to provide an analysis and summary of the surface reconstruction phenomenon specifically observed in perovskite oxides, considering both internal and external triggers that contribute to the structural changes.

5.1 Internal triggers

5.1.1 A-site elements

One common surface reconstruction phenomenon observed during OER is the surface amorphization resulting from the leaching of A-site metals. An example of this is the iridium oxide/strontium iridium oxide ($IrO_x/SrIrO_3$) catalyst studied by Thomas F. Jaramillo's group (Fig. 4 (a))[84]. In their work, thin films of $SrIrO_3$ were subjected to OER under acidic conditions, and the surface of the catalyst was characterized using XPS before and after the OER testing. The XPS analysis reveals that the Sr 3*d* peak could be fitted with two doublets prior to the OER testing. However, after the OER testing, only one doublet remains, accompanied by a decrease in signal intensity (Fig. 4 (b)). This observation indicates that the Sr metal in the A-site of $SrIrO_3$ thin film has leached out during the OER process. On the other hand, the Ir signals from XPS remain constant. Subsequently, the remaining iridium oxide undergoes structural changes and forms possible motifs such as IrO_3 or anatase IrO_2, as suggested by DFT calculations. This reconstructed surface exhibits remarkable activity, displaying an overpotential of only 270-290 mV when tested in an acidic electrolyte for a duration of 30 hours. However, the exact structure of the reconstructed surface during the reaction remains unknown.

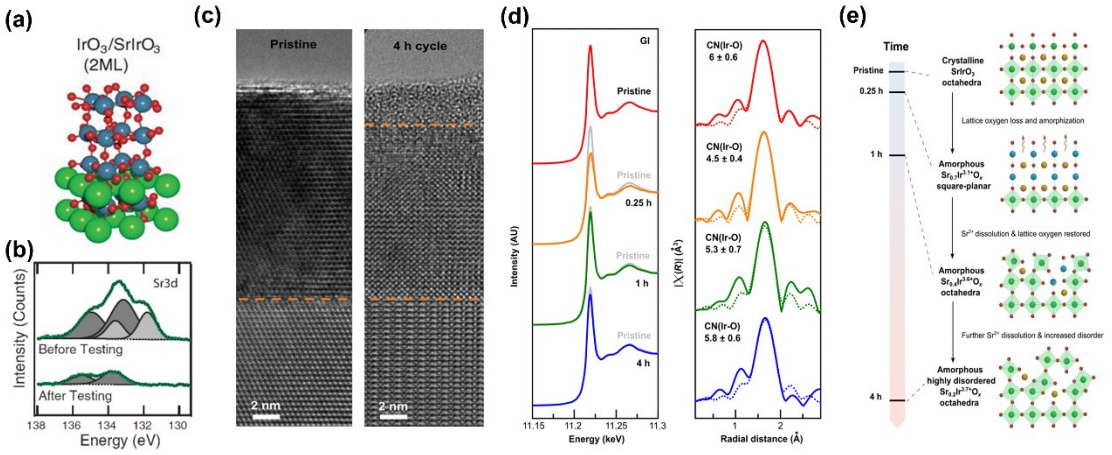

Figure 4. (a) Calculated $IrO_3/SrIrO_3$ surface structure model (green: Sr; blue: Ir; red: O) and (b) XPS spectra of Sr *3d* for $SrIrO_3$ films before and after OER testing[84]. (c) Cross section TEM images of $SrIrO_3$ (001) films before and after potential cycling for 4 hours[139]. (d) GI-XANES (left) and GI-EXAFS (right) of Ir L_3 before and after OER cycling[139]. (e) Proposed model for Ir formal oxidation sate evolution on $SrIrO_3$ film[139]. (a-b) Reproduced with permission[84]. Copyright 2016, the American Association for the Advancement of Science. (c-e) Adapted under CC BY-NC license from ref. [139].

Later, Wan et al. used electron microscopy and XAS to further study the surface reconstruction process of $SrIrO_3$ film during the OER process by taking lattice oxygen activation into account[139]. In 0.1 M $HClO_4$, the $SrIrO_3$ films were scanned by CV in the voltage range of 1.05 and 1.75 V. It was observed by cross-sectional TEM that after 4 h of CV scanning, an amorphous layer with a thickness of ~2.4 nm was formed on the crystalline $SrIrO_3$ as shown in Fig. 4 (c). With the further increase of CV scanning time, this amorphous layer provides protection against further amorphization of the underlying $SrIrO_3$. Analysis of the Sr L_3-edge XANES data was conducted in both total electron yield (TEY) mode (surface sensitive) and total fluorescence yield (TFY) mode (bulk sensitive). The results demonstrate an approximate 80% decrease in Sr content in the near surface and a 45% decrease in bulk Sr content after 4 hours of CV scanning. Simultaneously, the oxidation state of the near surface Ir decreases to 3.1 after 0.25 hours and subsequently increases to 3.7 (Fig. 4 (d), grazing incidence (GI)-XANES). Furthermore, the Ir-O coordination number reduces from the initial 6 to 4.5 after 0.25 hours, but then increases to 5.8 after 4 h (Fig. 4 (d), GI-EXAFS).

During the initial 2.5 h, the decrease of Ir-O coordination numbers indicates that lattice oxygen will also be lost accompanying the leaching of Sr to maintain charge

neutrality. The reduction of the oxidation state of Ir further indicates that lattice oxygen is leaving the amorphous layer to a greater extent than Sr. DFT calculations corroborate this observation by revealing a higher activation energy barrier (3.1 eV) for Sr migration compared to oxygen (1.9 eV). The subsequent increase in Ir-O coordination numbers and Ir oxidation state after 0.25 h suggests the refilling of oxygen vacancies to counteract Sr leaching. Based on these findings, a surface amorphization mechanism initiated by lattice oxygen activation was proposed (Fig. 4 (e)). The high oxidation potential activates lattice oxygen to form dioxygen firstly, resulting in the loss of lattice oxygen and the increase of oxygen vacancy. The newly formed oxygen vacancies then facilitate the diffusion of both O and Sr within the lattice. Due to this highly unstable structure, the crystalline $SrIrO_3$ surface reconstruct into an amorphous structure with a square-planar structure (0.25 h). The formation of this amorphous layer further induces significant leaching of Sr, destabilizing the defect-rich structure and causing the reoxidation of Ir through water oxidation. The coupled diffusion of Sr and O ultimately results in the formation of highly disordered Sr_yIrO_x species with a mixture of Ir(III) and Ir(IV) octahedral clusters, exhibiting high OER activity.

In contrast to the relatively stable bulk structure mentioned earlier, Ben-Naim et al. proposed a layer-by-layer degradation model for $SrIrO_3$ films at high oxidizing potentials (> 1.7 V)[140]. This model was supported by cross-sectional HR-TEM and helium ion microscope with secondary ion mass spectrometry (HIM-SIMS) analysis. As depicted in Fig. 5 (a), an initial SrO-rich surface was observed on the $SrIrO_3$ catalysts. During the OER treatment under acidic conditions, Sr leaches out from the surface, leading to the formation of an IrO_x-rich surface, while the bulk $SrIrO_3$ remains unchanged. Over time, the $SrIrO_3$ films measurably thin, and the active and fresh IrO_x-rich surface is continuously exposed throughout the entire OER process while maintaining its performance. Nanometer-resolution HIM-SIMS imaging displayed a uniform distribution of Sr and Ir elements on the surface and bulk of the reacted and thinned films, indicating that the IrO_x-rich layer possesses a partially crystalline nature (Fig. 5 (b)). HR-TEM images in Fig. 5 (a) further confirm the presence of crystalline domains, which could potentially correspond to a Sr-deficient perovskite structure or

IrO_3 with the WO_3 structure.

Song et al. conducted a study using STEM to investigate the dissolution-induced surface reconstruction of $AIrO_3$ (A = Sr or Ba) in an acidic electrolyte[141]. During anodic cycling, they observed leaching of Sr and Ba, along with surface roughening, in both $SrIrO_3$ and $BaIrO_3$. In Fig. 5 (c), the authors demonstrated that the current, normalized by the geometric area of the electrode, increases initially for the first 40 cycles and then decreases until reaching 130 cycles on $SrIrO_3$ films. Furthermore, in Fig. 5 (d), they found that the amorphous region expands with an increase in the number of scan cycles, consistent with the findings of Ben-Naim et al.[140]. After 130 scan cycles, the surface became almost entirely amorphous. Within the first 60 scan cycles, nanocrystals of rutile-type IrO_2 were observed near the surface region, as indicated by the measured interplanar spacing (refer to the enlarged images in Fig. 5 (d)). Remarkably, the surface roughening is associated with a significant increase in electrochemical active surface area (ECSA), which is believed to primarily contribute to the enhanced activity during the initial 40 scan cycles in $SrIrO_3$. However, the Tafel slopes remain unchanged, indicating no variation in the OER kinetics. Importantly, it should be noted that the normalized current by ECSA decreases with the increasing number of scan cycles for both $SrIrO_3$ and $BaIrO_3$, emphasizing the significance of surface roughening. The decline in activity and ECSA after 90 cycles is attributed to the slower loss of Ir compared to Sr. Specifically, the loss of Ir in $SrIrO_3$ is more pronounced than in $BaIrO_3$ due to the different IrO_6 connecting structures.

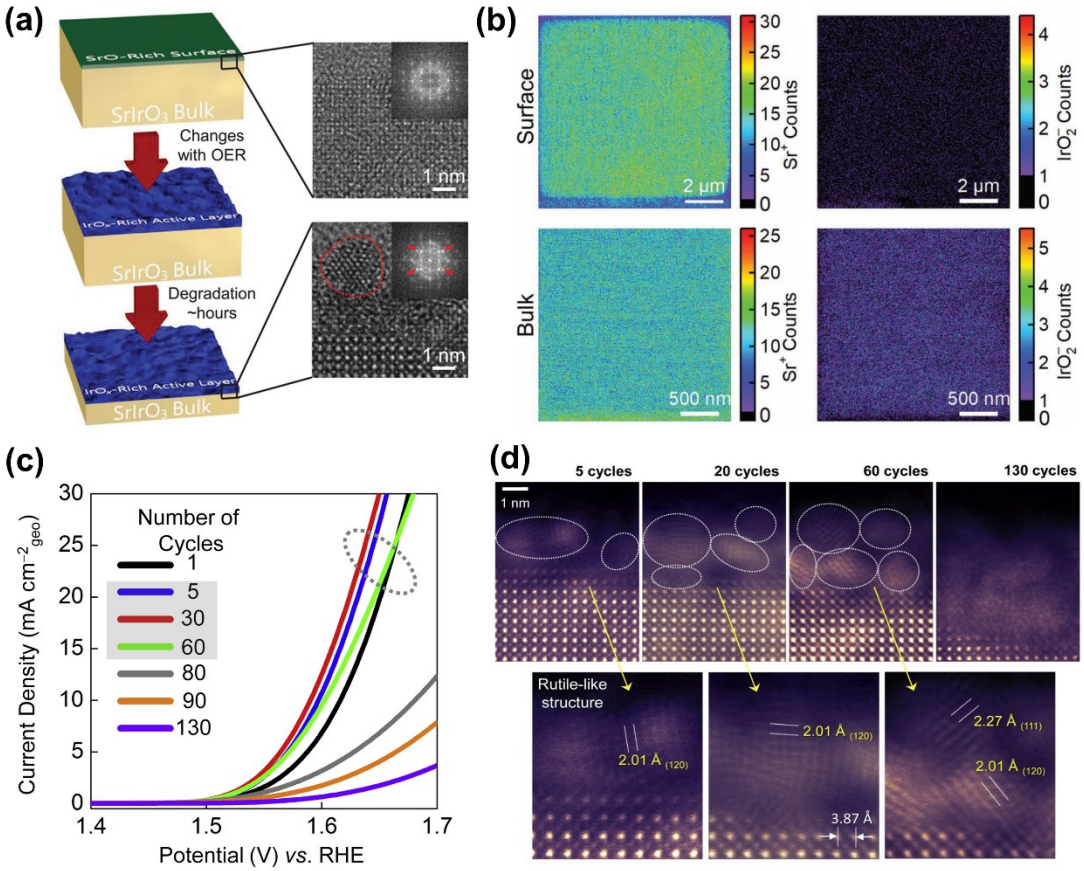

Figure 5. Surface reconstruction of $SrIrO_3$ film. (a) Degradation model of $SrIrO_3$ catalyst and the HR-TEM images before and after electrochemical reaction[140]. The red arrows in the inset FFT indicate the crystalline structure circled in red. (b) HIM-SIMS characterization of $SrIrO_3$|Nb:STO after high-potential testing. The upper images denote surface sensitive case while the bottom images denote bulk sensitive case[140]. The OER current densities (c) of thin $SrIrO_3$ film after different cycles and the corresponding HAADF-STEM images (d)[141]. The interplanar spacing values obtained are the same as those of the (120) and (111) planes in rutile IrO_2. (a-b) Reproduced with permission[140]. Copyright 2021, Wiley. (c-d) Reproduced with permission[141]. Copyright 2019, Elsevier.

In addition to $SrIrO_3$ catalyst, Sun et al. examined the phenomenon of surface reconstruction influenced by the doping of Ce into the A-site of $LaNiO_3$ catalysts[33]. Through in-situ Raman spectroscopy, they observed changes in the Raman peaks associated with $LaNiO_3$ as the applied potential increased from 1.0 to 1.4 V. The Raman peaks at approximately 211 and 426 cm^{-1}, attributed to $LaNiO_3$, gradually decrease in intensity. Upon further increasing the potential to 1.45 V, new Raman peaks emerge at around 475 and 551 cm^{-1}, corresponding to NiOOH, and their intensities increase with the applied potential. The introduction of Ce doping into $LaNiO_3$ results in a decrease in the surface reconstruction potential required for NiOOH formation. Specifically, at a

Ce doping ratio of 0.1, the surface reconstruction potential decreases from 1.45 V to 1.35 V. This A-site doping effect can be explained by the induction of oxygen vacancies caused by Ce doping, which enhances the structural flexibility and facilitates the formation of active (oxy)hydroxide species during surface reconstruction.

Samira et al. concluded that the extent of A-site cations leaching is correlated with the oxide crystal phase, oxide reducibility and the lattice strain induced by the differences in A-site cation size[142].

Another aspect related to surface reconstruction that can influence the OER is the preferential segregation of bivalent A-site cations in perovskite oxides to the surface, such as Sr-enriched layer on $SrTi_{1-x}Fe_xO_{3-\delta}$ electrodes[143] and Ba on $Ba_xSr_{1-x}Co_{0.8}Fe_{0.2}O_{3-\delta}$[144]. Zhu et al. discovered that on $Ba_xSr_{1-x}Co_{0.8}Fe_{0.2}O_{3-\delta}$, BaO and BaO_2 segregate on the surface under O_2-rich conditions at high temperatures, and these segregated species serve as active sites for the OER[144].

5.1.2 B-site elements

Although the octahedral structure of B-O_6 in comparison to A-site elements is generally stable during the OER process, there are circumstances in which leaching can occur. Notably, Ir[145], Sc[146], Co[146, 147], and Fe[147] have been observed to leach under certain conditions. Geiger et al. conducted an experiment in which they found that Ir dissolves in the range of 30-40 w% from the double perovskite oxide powder A_2BIrO6 (A=Ba, Sr; B=Nd, Pr, Y) in 0.1 M $HClO_4$ at open-circuit potential[145]. They proposed that non-noble metals dissolve initially, followed by the formation of isolated IrO_6 octahedra, which are prone to dissolution in the electrolyte. Consequently, the remaining structure collapses and transforms into amorphous iridium oxide. The dissolution of iridium in the perovskite structure is comparable to that of metallic iridium and hydrous iridium oxide, all of which exhibit orders of magnitude higher leaching rates than crystalline iridium oxide.

Chen et al. developed a pseudo-cubic perovskite material, $SrCo_{0.9}Ir_{0.1}O_{3-\delta}$, with corner-shared IrO_6 octahedrons[148]. Through XPS analysis, they observed the absence

of Sr *3d* and Co *2p* signals after electrochemical cycling, indicating their leaching from the material. HRTEM revealed the presence of an approximately 10 nm amorphous region on the surface, indicating surface reconstruction likely due to the leaching of Sr and Co. Later the same group extensively examined the influence of B-site cations on surface reconstruction, including metal leaching and the resulting structural rearrangement, using two model perovskites: $SrSc_{0.5}Ir_{0.5}O_3$ and $SrCo_{0.5}Ir_{0.5}O_3$[146]. Theoretical calculations initially predicted that the stability of the B-site cages, which consist of densely packed B-site octahedra, greatly affects the dissolution of A-site cations. Then experimental findings demonstrated that in the presence of 0.1 M $HClO_4$, Sr leaching in $SrCo_{0.5}Ir_{0.5}O_3$ was found to be higher than in $SrSc_{0.5}Ir_{0.5}O_3$, and Co is almost entirely leached out. Additionally, the reconstructed amorphous region of $SrCo0.5Ir_{0.5}O_3$ was observed to be deeper compared to $SrSc_{0.5}Ir_{0.5}O_3$, further supporting the role of B-site cations in influencing surface reconstruction. Furthermore, a comparison of intrinsic activity reveals that leaching of B-site cations initiates the formation of active IrO_xH_y, which exhibits a honeycomb-like structure, while Sr leaching in A-site primarily contributes to increase the ECSA for the reaction.

The surface reconstruction of BSCF under alkaline conditions during the OER was investigated using operando XAS, revealing dynamic characteristics[147]. Fig. 6 (a) illustrates the results obtained. When the applied potential increased from 1.2 to 1.425 V, no significant changes in the Co K-edge were observed, indicating a stable Co oxidation state. However, as the potential further increased to 1.55 V, a shift of the Co K-edge towards higher energy was observed, indicating an increase in the oxidation state. Simultaneously, an onset of OER current was detected within the same potential range. Interestingly, when the applied potential was returned to 1.2 V, no shift back of the Co K-edge was observed, suggesting that the oxidation of Co cations is an irreversible process. On the other hand, the valence state of Fe remained unchanged after the OER reaction. Fig. 6 (b) presents the results of operando Co-edge EXAFS. The first peak, associated with Co-O bonds and located at 1.8-2.0 Å, does not show significant changes with the applied potential. However, a splitting of the peak around 2.9 Å, corresponding to Co-Co/Fe coordination in the edge-sharing polyhedron, is

observed at 1.55 V. Additionally, an intensity increase in the split peak near 2.6 Å is attributed to the formation of CoOOH. Analysis of Fe K-edge EXAFS indicates the formation of FeOOH. Subsequent measurements at 1.2 V demonstrate that the split peaks do not revert back, further confirming its irreversible nature. Based on these results, a dissolution/re-deposition mechanism was proposed, leading to the formation of a self-assembled active surface layer consisting of CoOOH and FeOOH (Fig. 6 (c)).

Similar to the study of $SrIrO_3$[139], it was suggested that lattice oxygen evolution reaction (LOER) or LOM triggers the surface reconstruction in this case, as depicted by the following equation:

$$ABO_{3-\delta} + OH^- \leftrightarrow BOOH + A_{aq}^{2+} + \frac{2-\delta}{2} O_2 + 3e^- \quad (23)$$

According to the proposed equation, the Ba and Sr cations are dissolved in the electrolyte, whereas the low solubility of Co and Fe cations in an alkaline solution facilitates their re-deposition on the catalyst surface once they are dissolved. In this process, the released oxygen from the lattice can be replenished through the presence of OH^- ions in the electrolyte. These observations are supported by ICP results, which confirm that the leaching of Co and Fe is minimal, while the dissolution of Ba and Sr occurs to a significant extent.

Kim et al. conducted an analysis on the role of Fe in Co-based perovskites for the OER by comparing samples with and without Fe doping[149]. The inclusion of Fe in the perovskite structure was found to enhance both the activity and stability of the OER. Specifically, Fe doping contributes to stabilizing Co in a lower oxidation state, increasing the accessible surface area for the formation of the active (oxy)hydroxide layer, and expanding the potential range with improved thermodynamic metastability. The stabilization of Co in a lower oxidation state helps prevent the formation of undesired side oxides, minimizing their coverage on the surface. A perovskite with enhanced stability and coverage can serve as an effective substrate for the generation of the active layer. Fig. 6 (d) presents the results, where the two peaks around 2.8 Å and 3.0 Å correspond to the Co-Co coordination shells of CoOOH and the Co edge-sharing polyhedron, respectively, in line with previous assignments[147]. The plots of operando

difference spectra (dashed lines in Fig. 6 (d)) reveal a more pronounced increase in CoOOH formation (peaks around 2.8 Å) in BSCF compared to $Ba_{0.5}Sr_{0.5}CoO_{3-\delta}$ (BSC) as the applied potential increases. These results indicate that the potential-induced formation of the active (oxy)hydroxide layer is more prominent in BSCF than in BSC, particularly around the OER onset potential of approximately 1.4 V, which aligns with their respective OER activities. Importantly, it should be noted that Fe itself does not undergo significant changes during this study.

In an earlier study conducted by Risch et al., the investigation of $LaCoO_3$, $SrCo_{0.8}Fe_{0.2}O_{3-\delta}$, and BSCF using XAS revealed that the edge-sharing feature, with a distance of approximately 2.5 Å in EXAFS, can be introduced through ball milling and ink-casting in the synthesized BSCF material[22]. Fig. 6 (e) demonstrates that during electrochemical cycling between 1.1 and 1.7 V in 0.1 M KOH, the intensity of the corresponding peak around 2.5 Å increases with the number of cycles for $SrCo_{0.8}Fe_{e0.2}O_{3-\delta}$ and BSCF, while no change is observed for $LaCoO_3$. This increased peak is similar to that obtained for electrodeposited CoO_x, which serves as a model for the edge-sharing structure. Moreover, a decrease in the peaks at approximately 3.2 Å and 3.7 Å is noticeably observed for $SrCo_{0.8}Fe_{0.2}O_{3-\delta}$, indicating a change in the Co-A-site cation and Co-Co coordination in the corner-sharing octahedral, respectively, which is typical in perovskite structures. These findings suggest that electrochemical cycling induces a local structural transformation from corner-sharing octahedra to edge-sharing octahedra, accompanied by an increase in OER activity. The edge-sharing octahedra are envisioned as clusters with molecular dimensions, similar to electrodeposited metal oxides, and the formation of oxy(hydroxide) species is hinted as well. However, it is worth noting that the peak splitting phenomenon observed in BSCF in the aforementioned works was not observed in the work of Risch et al.[22].

Recently, the exposed surface metals (A or B site metals) in perovskite have been shown to dictate surface structure evolution by adopting operando UV–Vis spectroelectrochemistry[150]. Notably, in atomically flat $LaNiO_3$ thin films, the Ni-terminated surface exhibits a distinct optical density jump, coinciding with the potential where a redox feature is observed in CV. Conversely, such optical density changes are

absent on the La-terminated surface. Furthermore, this structural modification is associated with the evolution of a stable Ni hydroxide-like surface. The corresponding reconstructed surface reduces the overpotential of OER by up to 150 mV when compared to the La-terminated surface.

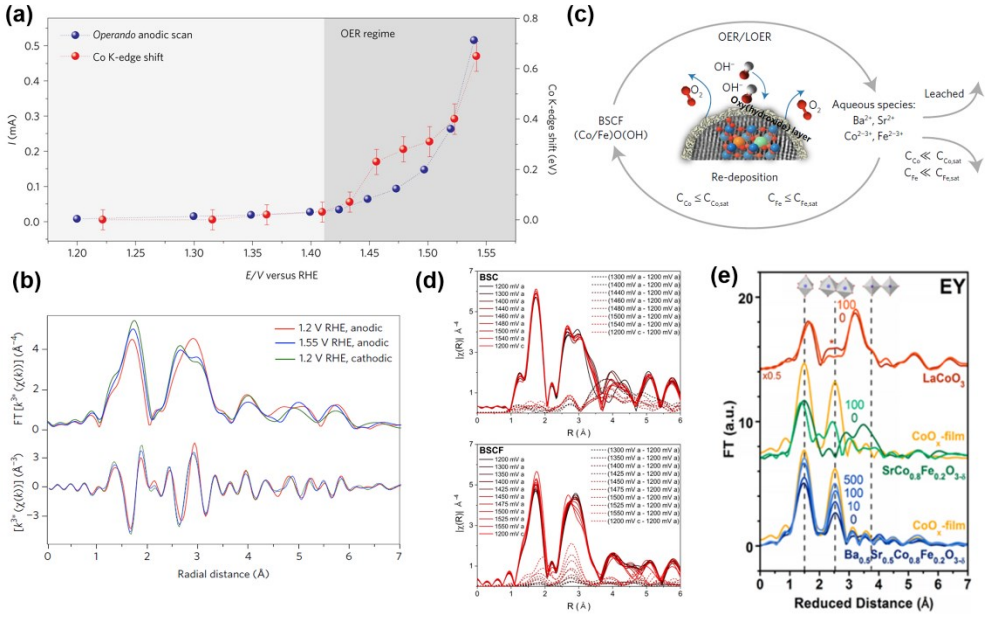

Figure 6. Surface reconstruction of BSCF. Operando XANES (a) and EXAFS (b) of BSCF in 0.1 M KOH [147]. During an anodic polarization, current and Co K-edge shift were recorded simultaneously. Co K-edge EXAFS spectra were analyzed by using Fourier transformed (FT) k^3-weighted method[147]. (c) Proposed dynamic surface self-reconstruction model via OER/LOER and dissolution/re-deposition mechanism[147]. (d) Operando FT k^3-weighted Co K-edge EXAFS spectra of BSC and BSCF[149]. (e) The FT EXAFS of $LaCoO_3$, $SrCo_{0.8}Fe_{0.2}O_{3-\delta}$ and BSCF before and after 100 (or 500) cycles. The electrodeposited CoO_x film was used as a reference. EY denotes electron yield signals which are surface sensitive[22]. (a-c) Reproduced with permission[147]. Copyright 2017, Springer Nature. (d) Reproduced with permission[149]. Copyright 2019, American Chemical Society. (e) Reproduced with permission[22]. Copyright 2013, American Chemical Society.

5.1.3 Lattice oxygen and oxygen vacancies

Lattice oxygen activation in the OER is a crucial factor in initiating the surface reconstruction process, as demonstrated by $SrIrO_3$ and BSCF. Theoretical studies have proposed the O-2p band center as a descriptor for determining surface stability and OER activity in perovskites[92]. Fig. 7 (a) illustrates the estimation of the O-*2p* band center by calculating the centroid of the projected density of states (PDOS) relative to the Fermi level. An overlap of transition metal *nd* and O-*2p* bands indicates the degree of hybridization of two bands and M-O bond covalency as well. This covalency has

been found to correlate well with OER activity in perovskite and other oxide materials[151-154]. In Fig. 7 (b), the upshift of the O-*2p* band center towards the Fermi level in double perovskites $(Ln_{0.5}Ba_{0.5})CoO_{3-\delta}$ leads to a decrease in the onset potential for OER, resulting from enhanced Co-O hybridization. However, further upshifting the O-*2p* band center does not result in a corresponding increase in activity. Instead, it leads to the amorphization of the catalyst surface in BSCF, $Ba_{0.5}Sr_{0.5}Co_{0.4}Fe_{0.6}O_{3-\delta}$ and $SrCo_{0.8}Fe_{0.2}O_{3-\delta}$. Consequently, an optimal covalency, as suggested by the O-*2p* band center, leads to the development of the best OER catalyst ($Pr_{0.5}Ba_{0.5}CoO_{3-\delta}$) in terms of both activity and stability and defines the boundary for surface reconstruction[92].

The covalency of the M-O bond is closely associated with the formation of oxygen vacancies, suggesting that a more covalent system indicates higher vacancy concentrations[155]. In a series of $La_{1-x}Sr_xCoO_{3-\delta}$ catalysts, the substitution of Sr^{2+} ions leads to an increase in the Co oxidation state from 3.0 to approximately 3.4, thereby enhancing the overlap between the Co *3d* and O *2p* bands, as well as increasing the covalency of the M-O bond. Consequently, the Fermi level decreases into the Co *3d*/O *2p* π^* band, facilitating the creation of oxygen vacancies[155]. Fig. 7 (c-d) further illustrates a linear correlation between the concentrations of oxygen vacancies (or the rate of oxygen diffusion) and the intrinsic OER activities in the $La_{1-x}Sr_xCoO_{3-\delta}$ catalysts, further emphasizing the significance of M-O bond covalency and supporting the mechanism of LOM. In this context, oxygen vacancy concentrations dictate the OER activity. However, if the lattice oxygen and water molecules are unable to replenish the surface oxygen vacancies in a timely manner (please see LOM in Fig. 1 (b)), the surface region may become unstable, leading to amorphization. Another study on $LaCo_{0.8}Fe_{0.2}O_{3-\delta}$ revealed that Sr doping induces the formation of oxygen vacancies and an amorphous layer, with the thickness of the layer increasing with higher Sr content[156]. This amorphous layer on the surface is considered the source of OER activity.

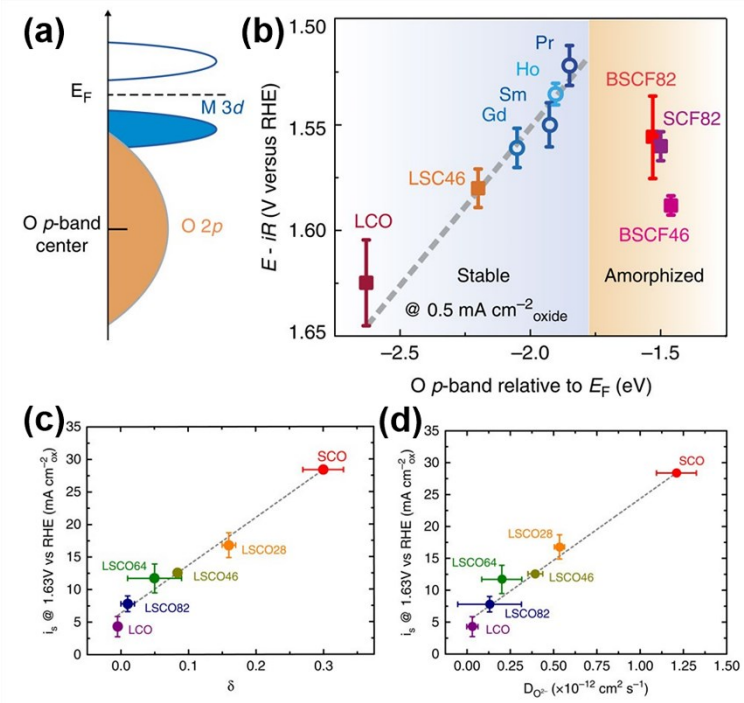

Figure 7. Effects of lattice oxygen and oxygen vacancies on OER activity and surface reconstruction. (a) Schematic drawing of the O *p*-band for transition metal oxides[92]. (b) The plot of the potential achieved at 0.5 mA cm_{oxide}^{-2} as a function of the O *p*-band center relative to fermi level E_F for $(Ln_{0.5}Ba_{0.5})CoO_{3-\delta}$ (Ln = Pr, Sm, Gd and Ho), $LaCoO_3$ (LCO), $La_{0.4}Sr_{0.6}CoO_{3-\delta}$ (LSC46), $Ba_{0.5}Sr_{0.5}Co_{0.8}Fe_{0.2}O_{3-\delta}$ (denoted as BSCF82 in the figure), $Ba_{0.5}Sr_{0.5}Co_{0.4}Fe_{0.6}O_{3-\delta}$ (BSCF46) and $SrCo_{0.8}Fe_{0.2}O_{3-\delta}$ (SCF82)[92]. Correlation of OER activity with oxygen vacancies δ (c) and oxygen ion diffusion rate (d) in a serials of $La_{1-x}Sr_xCoO_{3-\delta}$[61]. (a-b) Reproduced with permission[92]. Copyright 2013, Springer Nature. (c-d) Adapted under CC BY license from ref. [61].

5.2 External triggers

The surface of a catalyst can be significantly influenced by the applied test conditions, which can generally be categorized into two factors: electrochemical impact and chemical impact. The chemical impact primarily involves the influence of the electrolyte, including factors such as pH levels, electrolyte cations and impurities. On the other hand, the electrochemical impact pertains to the potential applied, which governs the thermodynamics and kinetics of electrochemical reactions, ultimately leading to surface reconstruction under specific pH conditions.

5.2.1 Applied potential

Pourbaix diagrams are useful tools that illustrate the thermodynamically stable phases of elements with different redox states in

aqueous solutions. These diagrams provide valuable insights into the stable species based on applied potential and pH. In a study by Raman et al.[157], surface Pourbaix diagrams were computed for $SrIrO_3$, $SrRuO_3$, and $SrTiO_3$ using a first principles approach. The computational findings revealed that under acidic conditions, the surface of $SrIrO_3$ transitions from a hydroxylated state to a fully oxidized state with a monolayer of adsorbed oxygen as the potential becomes more positive. Furthermore, the study demonstrated the formation of significant levels of Sr vacancies during the OER, leading to a reconstructed IrO_x-terminated surface, which is consistent with previous experimental observations[84].

In addition to computational approaches, experimental methods can also be employed to construct iridium Pourbaix diagrams[158]. Under acidic conditions, the precipitation of active $IrO_x \cdot mH_2O$ is indicated following the dissolution of metals, which has been observed in the investigation of $Sr_2MIr(V)O_6$ (M=Fe, Co) and $Sr_2Fe_{0.5}Ir_{0.5}(V)O_4$. More specifically, the open circuit potentials of Sr_2FeIrO_6 and $Sr_2Fe_{0.5}Ir_{0.5}O_4$ are found to be lower than the precipitation potential of $IrO_x \cdot mH_2O$. As a result, these compounds initially exhibit low activity for the OER due to their intrinsic perovskite activity. However, over time, their OER activity increases as electrodeposited $IrO_x \cdot mH_2O$ forms on the surface. Under alkaline conditions, soluble iridium species such as $Ir(OH)_6^{2-}$ or $Ir(OH)_2(ClO_4)_4^{2-}$ are favored during OER.

Fig. 8 (a-b) depicts Pourbaix diagrams of $SrRuO_3$ and $LaRuO_3$ assisted by DFT calculations[159]. When considering the working conditions (represented by vertical lines in Fig. 8(a-b)), the diagrams clearly show the dissolution of Sr^{2+} and La^{3+} ions, as well as La-containing aqueous species. This indicates that the surface of these perovskites is generally unstable under most investigated conditions. Notably, a phase transition from RuO_2 to RuO_4 occurs alongside the dissolution of Ru species at around 1.3 V, which is close to the onset potential of the OER. This highlights the

significance of this phase transition in influencing OER. In Fig. 8 (c), the Pourbaix diagram of BSCF is depicted[160]. Similar to $SrRuO_3$ and $LaRuO_3$, dissolutions of Ba^{2+} and Sr^{2+} species were observed under working conditions (E=1.0-1.7 V; pH=13), while the overall perovskite structure remains intact. Moreover, another thermodynamic calculation, which considers the lattice oxygen evolution reaction, reveals that metal oxides cannot remain stable under OER conditions regardless of the electrolyte's pH[65]. This instability arises from the thermodynamic properties of the oxygen anion within the metal oxide lattice. It is important to note that this finding does not contradict the Pourbaix diagram, as the diagram typically does not account for the evolution of oxygen from the lattice.

Different applied potentials induce distinct structural evolution processes[161]. As mentioned previously, electrochemical cycling leads to surface reconstruction of BSCF[21]. The as-prepared BSCF demonstrates a broad peak at approximately 675 cm^{-1}, attributed to the internal motion of oxygen within the CoO_6 and FeO_6 octahedra[21, 162]. Upon reaching 50 cycles, the Raman feature shows minimal changes within the cycling potential range of 0.7 to 1.0 V, as well as 1.1 to 1.5 V. However, when cycling between 1.5 and 1.7 V, triggering the OER process, a drastic reduction in Raman intensity is observed. This suggests that surface amorphization rapidly occurs when the potential exceeds 1.5 V.

Moreover, operando liquid phase TEM analysis has provided insights into the potential-dependent structural evolution of BSCF[163]. Fig. 9 (a) illustrates the reversible phenomenon observed during electrochemical cycling, where a dense cloud surrounding the particles initially appears and then diminishes over time. The variations in cloud length are attributed to fluctuations in the liquid that wets the BSCF particles. Essentially, the different applied potentials induce dynamic movement of the liquid, resulting in contrasting images in TEM.

To depict the relationship between applied potential and cloud length,

a plot of the one-dimensional cloud length normalized by its initial value is presented in Fig. 9 (b). Based on the curve characteristics, three distinct potential regions can be identified: a low potentials region (<1.2 V), intermediate potentials region (1.2-1.65 V), and high potentials region (>1.65 V). In each region, the evolved structure differs, influencing the wettability of BSCF particles and subsequently altering the liquid movement on the surface, ultimately leading to changes in liquid thickness and contrast in the TEM image.

In the low application potential region, a thin layer of OH^- accumulates at the interface, causing the surface to transition from a hydrophobic to a hydrophilic state. At 1.2 V, an (oxy)hydroxide phase forms, further enhancing the hydrophilic wetting behavior. Additionally, the hydrophilicity of BSCF remains relatively stable until 1.65 V, where oxygen gas evolution occurs. The evolved gas reduces the thickness of the liquid layer. It is worth noting that the potential for (oxy)hydroxide formation on BSCF is estimated to be 1.2 V in this study, below which the OER current is initiated.

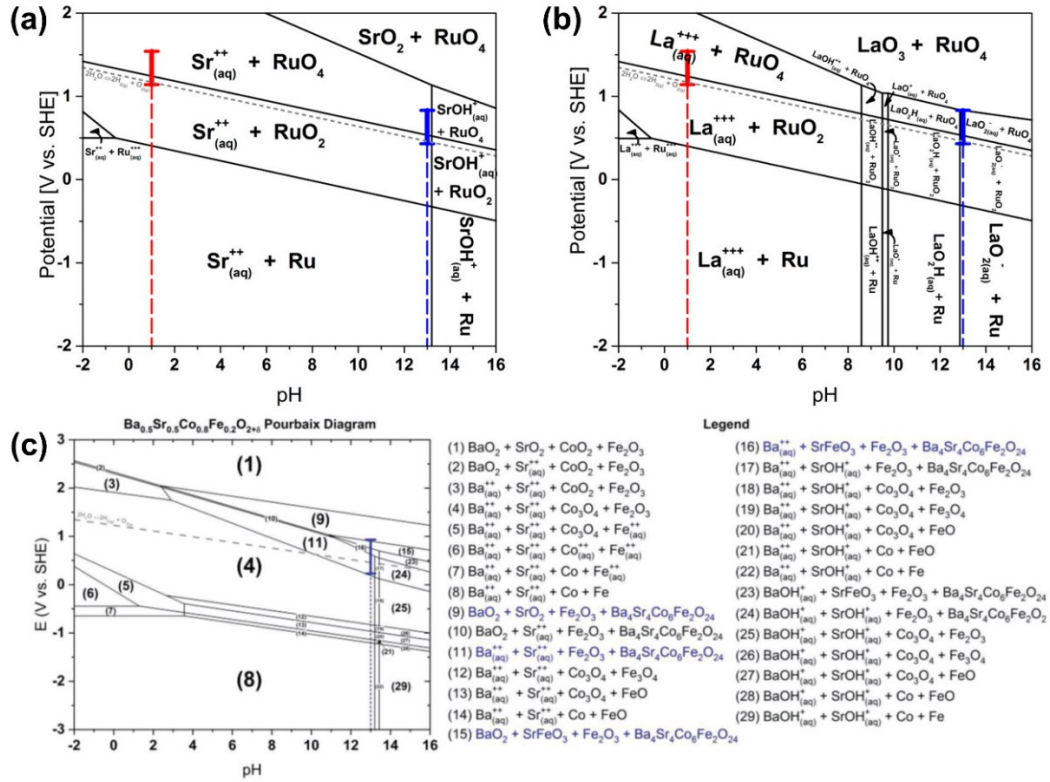

Figure 8. Pourbaix diagrams of (a) $SrRuO_3$[159]; (b) $LaRuO_3$[159]; and (c) BSCF[160]. (a-b) Reproduced with permission[159]. Copyright 2017, American Chemical Society. (d) Reproduced with permission[160]. Copyright 2018, Wiley.

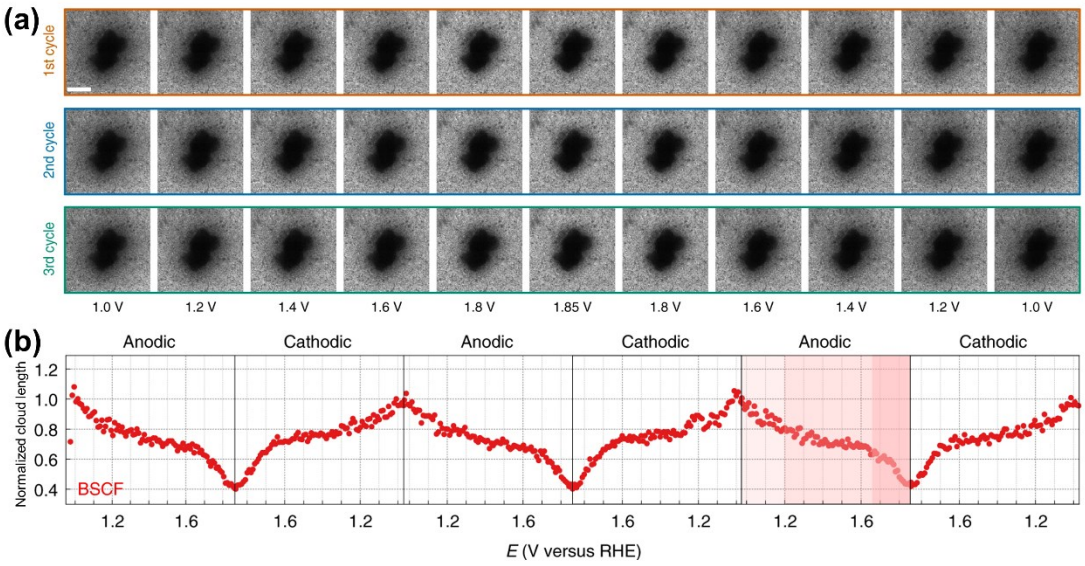

Figure 9. Effects of applied potential on surface reconstruction. (a) Real-time TEM images of BSCF particle during CV test[163]. (b) Plot of normalized cloud length as a function of applied potential in the first three cycles. The cloud length was normalized to its value at initial state (1.0 V)[163]. (a-b) Adapted under CC BY license from ref. [163].

5.2.2 Electrolyte pH

In general, electrolyte pH can affect the electrocatalytic process via modulating the proton donor (H_3O^+ or H_2O), adsorbate dipole-filed interaction, solution phase reactions with OH^-[164]. Consequently, the electrolyte pH can induce a shift in the reaction mechanism, either towards a proton-coupled electron transfer reaction or a decoupled one, depending on the specific conditions[36, 45, 93, 165, 166]. Moreover, the pH of the electrolyte also has an influence on the catalyst side, such as surface reconstruction during the OER.

Kim et al. studied the OER performance of six different perovskite oxides, namely $Ba_{0.5}Sr_{0.5}CoO_{3-\delta}$ (BSC), BSCF, $La_{0.5}Sr_{0.5}CoO_{3-\delta}$ (LSC), $La_{0.2}Sr_{0.8}Co_{0.8}Fe_{0.2}O_{3-\delta}$ (LSCF), $PrBaCo_2O_{6-\delta}$ (PBC), and $PrBaCo_{1.6}Fe_{0.4}O_{6-\delta}$ (PBCF) in neutral to alkaline media[167]. The results depicted in Fig. 10 (a) demonstrate that all tested perovskites, except for BSCF at pH 13, experience a decline in activity at the tested pH levels. This suggests that BSCF at pH 13 is the only metastable structure among the investigated materials. Interestingly, the logarithm of activity exhibits distinct trends with respect to pH, differentiating between the near-neutral region (pH 7-9) and alkaline conditions

(pH 12-14). This distinction implies that the dominant reaction mechanism may vary at different pH levels. Additionally, the study revealed that the potential-induced increase in the oxidation state of Co only occurs under alkaline conditions (pH 13) for BSC and BSCF. This observation is supported by the shift in the Co K-edge position in operando XANES spectra, as illustrated in Fig. 10 (b). The increase in Co oxidation state beyond the OER onset potential (1.4 V) is attributed to the formation of active (oxy)hydroxides, as indicated by EXAFS data, aligning with previous findings[147]. These findings suggest that the pH environment influences the preference for either the LOM or the conventional AEM mechanism. Specifically, under alkaline conditions, LOM is favored, leading to the formation of active (oxy)hydroxides and enhanced OER activity. However, at neutral pH, the formation of an oxy(hydroxide) layer is less pronounced, as evidenced from negligible changes in the Co K-edge position and EXAFS spectra.

Crystalline and amorphous metal oxides have been shown to respond differently at distinct electrolyte pH levels. In a study by Yang et al.[168], two types of nickel-based crystalline oxides, $LaNiO_{3-\delta}$ and $La_2Li_{0.5}Ni_{0.5}O_{4\pm\delta}$ (LLNO), were compared with amorphous Ni-Fe (oxy)hydroxide to investigate the influence of pH on OER activity and surface stability of nickel-based catalysts. The OER activity of the two crystalline nickel-based oxides was found to increase with increasing electrolyte pH, while it remained relatively constant for the amorphous catalyst. Fig. 10 (c) illustrates that as the electrolyte pH increased from 12.5 to 14, the thickness of the amorphous layer of LLNO grows from approximately 2 to 6 nm after 30 CV cycles. This growth can be attributed to the leaching of Li, La, and Ni cations. The mass loss of LLNO, as determined by electrochemical quartz crystal microbalance (EQCM), was observed to be significant and increased with higher electrolyte pH, which aligns with electron microscopy observations. In comparison, the mass losses of $LaNiO_{3-\delta}$ and Ni(Fe)OOH are relatively limited. Fig. 10 (d) presents the collection efficiencies ($\eta = i_{ring}/i_{disk}$) obtained from RRDE measurements for the three catalysts as a function of scan cycles at different pH levels. It was observed that the collection efficiency for both LLNO and $LaNiO_{3-\delta}$ decreased with increasing electrolyte pH, while the collection efficiency for Ni(Fe)OOH remained relatively stable at the tested pH values, reaching approximately

10%. These results indicate that the crystalline nickel-based perovskites exhibit an enhanced degradation process (low collection efficiency) at high pH levels compared to the amorphous catalyst. This difference has a significant impact on the activity behaviors of the catalysts at different pH levels.

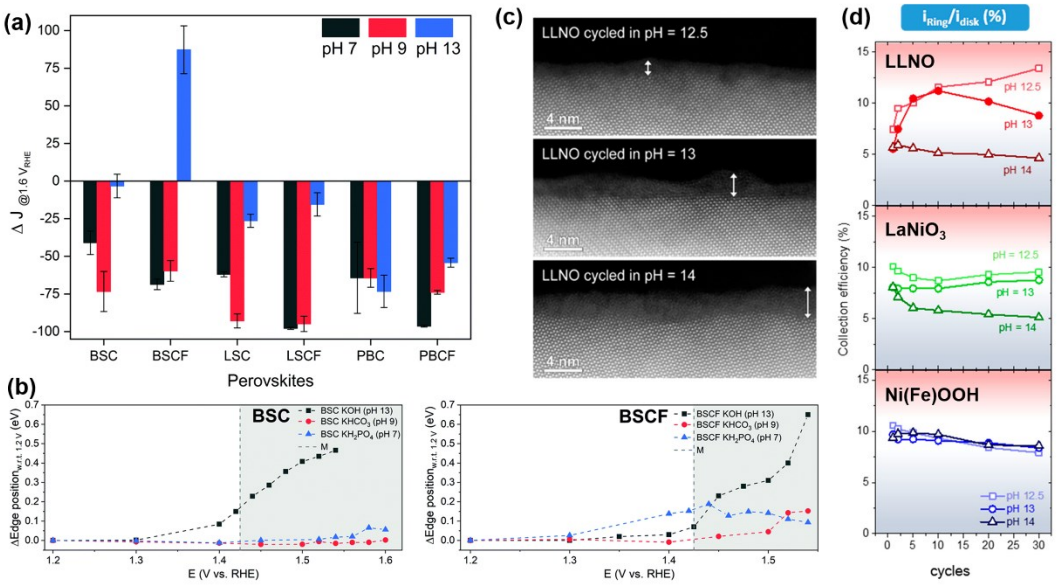

Figure 10. Effects of electrolyte pH on surface reconstruction. (a) Comparison of current changes measured at 1.6 V after 500 CV cycles from 1.0 to 1.6 V at pH = 7, 9, and 13[167]. (b) Operando XAS measurements of BSC and BSCF at different pH levels. The Co K-edge shift at specific potential was measured with respect to the edge position at 1.2 V [167]. (c) HAADF-STEM images of the CV cycled LLNO catalyst at different pH levels[168]. (d) The collection efficiencies ($\eta = i_{ring}/i_{disk}$) obtained at various pH levels as a function of cycling number for the three nickel-based catalysts: LLNO, $LaNiO_{3-\delta}$, and Ni(Fe)OOH[168]. (a-b) Adapted under CC BY-NC 3.0 license from ref. [167]. (c-d) Reproduced with permission[168]. Copyright 2018, American Chemical Society.

5.2.3 Electrolyte cation

One of the most well-known cation effects observed in electrolytes is the "Fe effect" in OER research, which is often difficult to avoid when using commercially supplied materials[169]. The Boettcher group identified the Fe effect in enhancing OER activity on a $Ni(OH)_2$ electrode by developing a method to absorb all Fe impurities in the electrolyte through the use of precipitated $Ni(OH)_2$ powder[170]. The Bell group further confirmed that the active site for OER is actually the Fe site within the NiOOH structure, which can be formed through the oxidation of $Ni(OH)_2$[171, 172]. These

findings suggest that previous reports attributing the high activity of $Ni(OH)_2$ catalysts to intrinsic properties are likely influenced by the presence of Fe impurities. Recently, a dynamic active site generated from the dissolution and redeposition of Fe over a MO_xH_y host has been proposed, emphasizing the importance of the Fe-M adsorption energy. This dynamic perspective provides a deeper understanding of the Fe effect on the formation of active sites, in contrast to static models[173].

In a subsequent study, the same research group extended their investigation of dynamic active site formation to $La_{1-x}Sr_xCoO_3$ perovskite oxides in the presence of aqueous Fe ions[174]. Surprisingly, they found that the OER activity of $La_{1-x}Sr_xCoO_3$ after 50 potential cycles was significantly higher in the presence of only 0.1 ppm Fe ions compared to purified KOH electrolyte (Fig. 11 (a)). In the purified KOH solution, the OER activity of $La_{1-x}Sr_xCoO_3$ is independent of the potential cycle and Sr content. While the OER activity increase gains more for samples with higher Sr content in the presence of Fe ions after a certain number of potential cycles. When the scan cycles are increased to 2000, all samples eventually exhibit similar OER activity. This suggests that a higher Sr content in perovskites leads to faster activation with the assistance of Fe impurities. These findings indicate that the surface reconstruction to form an active site is influenced by Fe impurities and Sr dissolution. Additional information from electron microscopy and ICP-MS analysis support the proposal of a dynamically stable active site containing Fe, which evolves through the interaction of aqueous Fe ions and a CoOOH shell supported on perovskites ((Fig. 11 (b)). The preference for Fe interaction with CoOOH over perovskite is also supported by DFT calculations (-1.4 eV vs. -0.55 eV). According to this model, the observed activity-pH relationship mentioned earlier is simply a result of Fe dilution at lower pH levels. As shown in Fig. 11 (c), the OER activity of $La_{0.7}Sr_{0.3}CoO_3$ is independent of pH in the absence or presence of Fe (with controlled concentration). However, the activity varied in commercial KOH with different pH values due to the dilution effect of Fe in the prepared electrolyte.

The presence of the Fe effect was also demonstrated in $SrCoO_{3-\delta}$ by comparing it with $SrCo_{0.8}Fe_{0.2}O_{3-\delta}$[175]. The similar OER activity observed for $SrCoO_{3-\delta}$ with

spiked Fe^{3+} and $SrCo_{0.8}Fe_{0.2}O_{3-\delta}$ suggests that the remaining bulk structure has a limited effect on the formation of the active structure. This may imply that the Fe effect in enhancing OER activity is primarily influenced by surface interactions rather than the bulk structure.

Furthermore, another electrolyte cation effect has been recently revealed in $SrCoO_{3-\delta}$, known as backfilling of electrolyte cations with smaller size (e.g., Na^+), which occurs within the cationic vacancy on the catalyst's surface. This process stabilizes the reconstructed framework of the catalyst, leading to greatly improved OER performance[176].

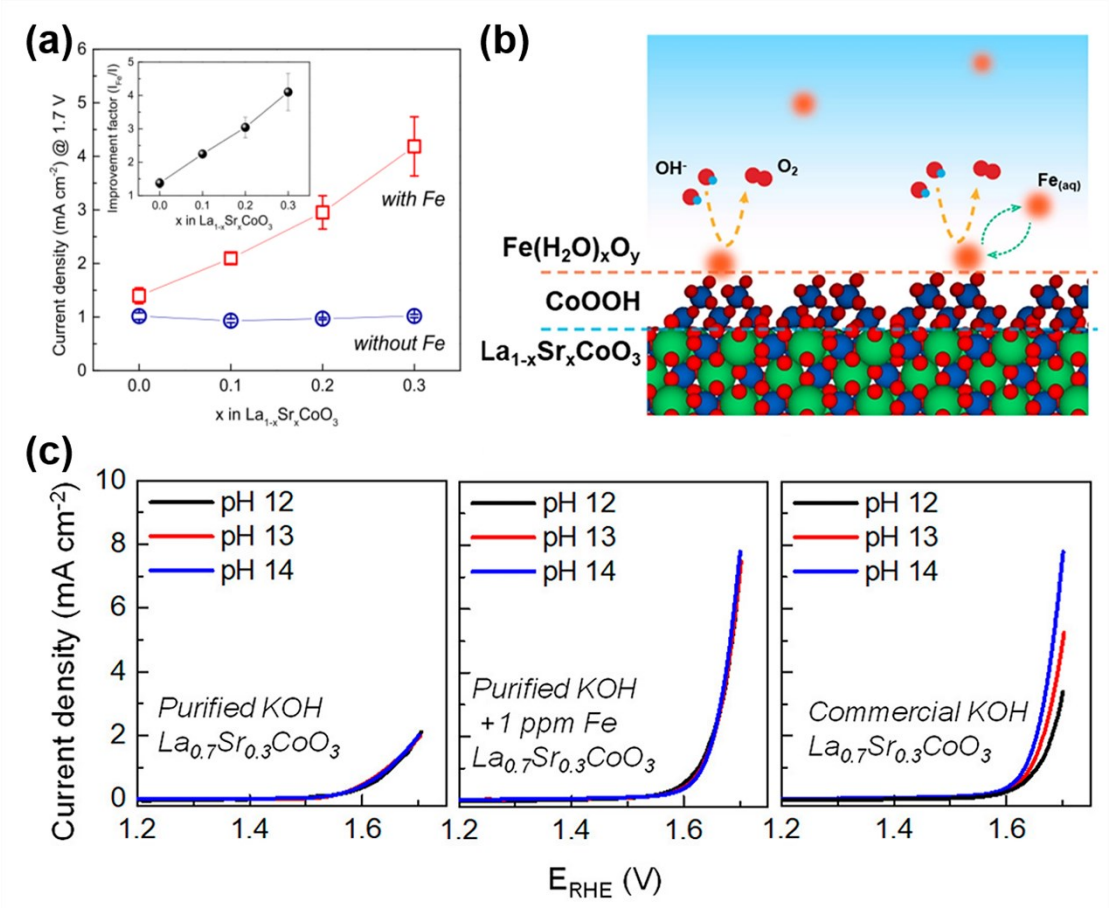

Figure 11. Effects of Fe impurities on surface reconstruction. (a) Comparison of OER current density (50th cycle) measured at 1.7 V as a function of the Sr-doping levels in $La_{1-x}Sr_xCoO_3$ in the absence/presence of 0.1 ppm aqueous Fe ion. Inset shows the O_2 production rate enhancement with and without Fe[174]. (b) Schematic illustration of the core−shell interface structure formed over $La_{1-x}Sr_xCoO_3$ in the presence of Fe[174]. (c) OER polarization curves of $La_{0.7}Sr_{0.3}CoO_3$ measured at different pH levels after activation in purified KOH, purified KOH with controlled Fe content, and commercial KOH[174]. (a-c) Reproduced with permission[174]. Copyright 2021, American Chemical Society .

5.2.4 Chemical immersion

The electrochemical study sometimes overlooks the effects of pure chemical reactions. Recent research has highlighted that the immersion of electrode catalysts in acidic or alkaline electrolytes alone can have impacts on surface reconstruction. An example of this phenomenon can be observed when Ir^{V}-based perovskite oxides are soaked in a 0.1 M $HClO_4$ solution, resulting in a distinctive purple-pink coloration[158]. This change in color corresponds to the presence of a soluble iridium species, as indicated by a broad absorption peak observed at approximately 520 nm in the UV-Vis spectra. To further investigate the impact of chemical and electrochemical factors, the authors conducted a comparison by immersing iridium-based catalysts in an acidic electrolyte, both with and without the application of potentials. Thus, in certain catalysts, the dissolution experienced in the chemical environment was found to be more severe compared to that in the electrochemical environment.

In a study by Shen et al., it was reported that the surface of as-synthesized BSCF is surrounded by a secondary phase rich in Ba and Sr[177]. This secondary phase can be observed in the indicated region by white arrows in Fig. 12 (a). However, after immersing BSCF in a 0.1 M KOH solution for 3 hours, the secondary phase is removed, revealing a spinel-like Co/Fe-rich shell (Fig. 12 (a)). The assignment of this spinel-like structure is supported by key results from O-K edge and Co-L_3 edge spectra, as well as FFT analysis of TEM images on the surface. In contrast to previous proposed mechanism of (oxy)hydroxide formation from BSCF itself, the spinel-like structure with Co^{2+} is thought to be the precursor to transform into the active CoOOH (Fig. 12 (b)). Additionally, the study found that the Co^{2+}/Co^{3+} redox transition is reversible, which differs from the finding of irreversible oxidation of Co in another report[147]. On the other hand, Jung et al. discovered that heat treatment in an oxygen environment can remove the inherent surface spinel phase layer on BSCF, leading to increased crystallinity and improved catalytic activity for the OER[178].

Chemical immersion has been demonstrated to be able to increase the OER activity of BSCF[179]. The increase ratio, defined as the OER current

enhancement at 1.7 V during the second CV cycle compared to the first cycle, was used to evaluate the activity improvement. Between the two cycles, there are chemical immersion for different time in 1.0 M KOH. Fig. 12 (c) shows that as the immersion time in 1.0 M KOH increases, the increase ratio also increases, indicating that chemical immersion effectively enhances the OER activity of BSCF. However, it is worth noting that the OER enhancement achieved through chemical immersion was still lower compared to that obtained through electrochemical cycling for the same duration (100 min, as shown in Fig. 12 (c)). Additionally, the Raman peak at approximately 675 cm^{-1}, which nearly disappears under electrochemical conditions, remained but became broader after immersing BSCF in 1.0 M KOH for 120 min (Fig. 12 (d))[21]. This result suggests that the degree of surface amorphization resulting from chemical immersion is lower compared to that from electrochemical treatment, which aligns with the pattern observed in the increase ratio. Interestingly, the degrees of metal dissolution from the A and B-sites of BSCF were comparable after chemical immersion or OER cycling, indicating that the dissolution of metals from BSCF is primarily influenced by chemical effects rather than electrochemical processes (Fig. 12 (e)).

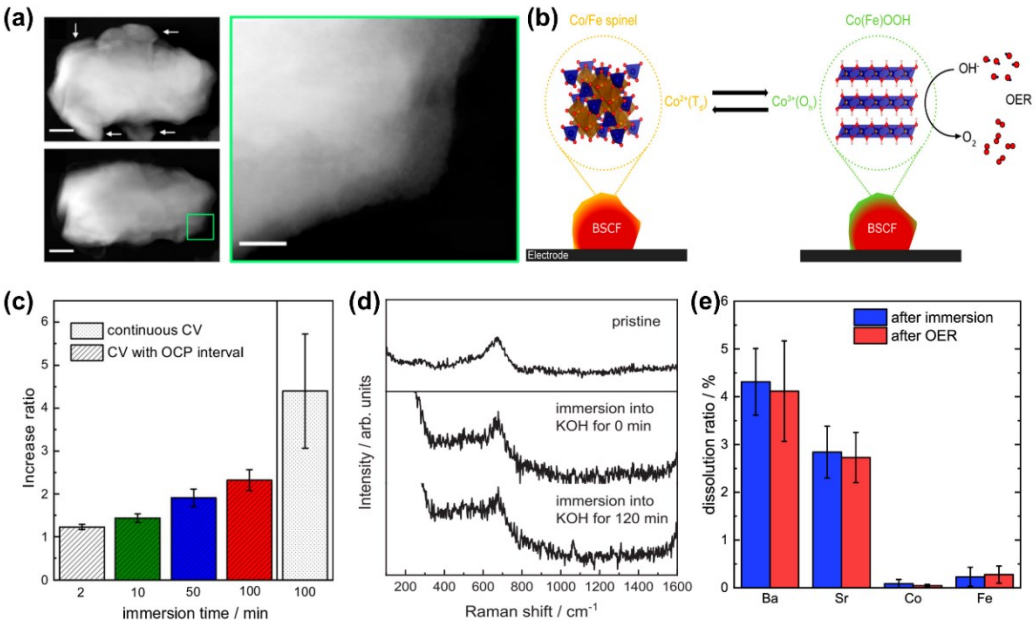

Figure 12. Effects of chemical immersion on surface reconstruction. (a) HAADF-STEM images of original BSCF particles (upper-left) and images (lower-left and right) after soaking in KOH for 3 hours. The right figure in the green square denotes the enlarged one of the lower left figure[177]. (b) Surface reconstruction model for reversible formation of Co/Fe (oxy)hydroxide on the spinel-like surface of BSCF[177]. (c) Increase ratio of OER currents for different chemical immersion time. The result from continuous CV cycles, which corresponds to 100 min, is shown for comparison (column in the right end)[179]. (d) In-situ Raman spectra of BSCF before and after immersion in 1 M KOH solution[179]. (e) Dissolution ratios of metal elements of BSCF in the electrolyte as determined from ICP-OES after immersion and OER cycling[179]. (a-b) Adapted under an ACS AuthorChoice license from ref. [177]. (c-e) Reproduced with permission[179]. Copyright 2022, IOP.

5.3 Proposed reconstructed structures

The studies mentioned above have highlighted the dynamic surface reconstructions that perovskite oxides undergo under reaction conditions, which are closely related to the formation of active sites. Several research studies have investigated and identified the evolved surface structures using various characterization techniques, including in-situ and operando methods. Table 1 summarizes the findings from the literature regarding the identification of evolved surface structures in perovskite systems. For example, in the case of $SrIrO_3$, a simple perovskite system, leaching of A-site metals under acidic conditions typically leads to the formation of an active layer consisting of amorphous IrO_x on the surface. On the other hand, for Co/Fe-based perovskites, the surface reconstruction process involves both the leaching of A-

site metals and the re-deposition of dissolved B-site cations under alkaline conditions. This reconstruction process results in the formation of a dynamically stable Co/Fe (oxy)hydroxide active layer, as proposed in the majority of the literature. Overall, these findings suggest that the as-synthesized perovskite itself should be regarded as a "pre-" catalyst, and the active surface structure evolves during the catalytic process.

Table 1. Literature summary of proposed reconstructed surface structures from perovskite oxides during OER process

Pre-catalysts	Reconstructed surface structure	Overpotential	Electrolyte	Characterization tools	Reference
$SrIrO_3$	IrO_x	270–290 mV (@10 mA·cm_{ox}^{-2})	0.5 M H_2SO_4	XPS	[84]
$SrIrO_3$	Sr_yIrO_x	/	0.1 M $HClO_4$	TEM; XAS	[139]
$SrIrO_3$	IrO_x	/	0.5 M H_2SO_4	HR-TEM; HIM-SIM; XAS	[140]
A_2BIrO_6 (A=Ba, Sr; B=Nd, Pr, Y)	Isolated IrO_6 octahedra	/	0.1 M $HClO_4$	XPS	[145]
$AIrO_3$ (A=Sr, Ba)	Rutile-like IrO_x	/	0.5 M H_2SO_4	HAADF-STEM	[141]
$SrCo_{0.9}Ir_{0.1}O_{3-\delta}$	IrO_x octahedra	270 mV (@2.8 mA·cm^{-2})	0.1 M $HClO_4$	XPS; XAS	[148]
$SrSc_{0.5}Ir_{0.5}O_3$	Honeycomb-like IrO_xH_y	$HClO_4$: 250–263 mV (@TOF=0.03 s^{-1})	0.1 M $HClO_4$; 0.1 M KOH	XAS; EELS	[146]
$SrCo_{0.5}Ir_{0.5}O_3$	Honeycomb-like IrO_xH_y	$HClO_4$: 250–263 mV ; KOH: 308–315 mV (@TOF=0.03 s^{-1})	0.1 M $HClO_4$; 0.1 M KOH	XAS; EELS	[146]
$SrCo_{0.8}Fe_{0.2}O_{3-\delta}$	Edge sharing CoO_6	/	0.1 M KOH	EXAFS	[22]
BSCF	Edge sharing CoO_6	/	0.1 M KOH	EXAFS	[22]
BSCF	(Co/Fe)OOH	/	0.1 M KOH	operando XAS	[180]
BSCF	(Co/Fe)OOH	/	0.1 M KOH	operando XAS	[147]
BSCF	Co(Fe)OOH	/	0.1 M KOH	operando liquid TEM;	[163]
BSCF	Co(Fe)OOH	/	0.1 M KOH	in-situ TEM	[177]
$LaCo_{0.8}Fe_{0.2}O_{3-\delta}$	(Co/Fe)OOH	293 mV (@10 mA·cm^{-2})	0.1 M KOH	operando XAS	[32]
$La_{1-x}Ce_xNiO_3$	NiOOH	$La_{0.9}Ce_{0.1}NiO_3$: 270 mV (@10 mA·cm^{-2})	1 M KOH	in-situ Raman	[33]
$La_{0.2}Sr_{0.8}Co_{0.8}Fe_{0.2}O_{3-\delta}$	~6 nm amorphous layer	350 mV (@10 mA·cm^{-2})	0.1 M KOH	XAS; HRTEM	[156]
$LaLi_{0.5}Ni_{0.5}O_4$	Amorphous	/	pH=12.5, 13, 14 KOH	HAADF-STEM; XAS	[168]
$La_{1-x}Sr_xCoO_{3-\delta}$	CoO_xH_y	/	pH=12, 13, 14 KOH	SERS; in-situ ICP-MS;	[174]
$LaNiO_3$	NiOOH type surface layer	0.5–0.6 V (@1 mA·cm^{-2})	0.1 M KOH	operando UV-Vis	[150]
$Ba_xSr_{1-x}Co_{0.8}Fe_{0.2}O_{3-\delta}$	BaO, BaO_2	/	/	In-situ TEM; UV-Raman	[144]

6. Concluding remarks and outlook

In this review, we critically examine the results of the past decade related to the surface reconstruction of perovskite oxides during the OER. Through the integration of advanced characterization tools and theoretical methods, particularly focusing on DFT calculations, substantial insights have been gained. These insights highlight the crucial influence of factors such as composition, surface structure, and potentially bulk structure, as well as test conditions, on the surface reconstruction of perovskites during the OER process. Yet the correlation between evolved structure and OER performance, including activity and stability, is far from complete understanding, which poses a significant challenge in the rational design of catalysts. The detailed OER mechanism and quantification on the contribution of both proposed mechanisms over the reconstructed surface is still elusive.

6.1 Exploring the vast chemical space of perovskites aided by machine learning methods. It is a challenging task due to the diverse range of A and B-site metals available and the complex structural arrangements they can form. As a result, many properties of hypothetical perovskites remain unknown. The catalyst library studied thus far has primarily focused on B-site metals such as Ir, Ru, Fe, Co, and Ni. However, it is highly desirable to expand the range of compositional elements, particularly by incorporating abundant and cost-effective alternatives to Ir and Ru. Nonetheless, preparing and testing all possible perovskite compositions and structures would be prohibitively expensive and time-consuming. Fortunately, machine learning methods have emerged as powerful tools in catalyst research over the past decade. They offer a means of conducting high-throughput screening of perovskite catalysts effectively[181, 182]. By utilizing machine learning algorithms, researchers can select the most promising ones for further testing and characterization. This approach significantly accelerates the exploration of the perovskite chemical space and enhances our understanding of the structure-performance relationship in a wider context.

6.2 Utilizing combinational operando characterization tools for active structure determination. Despite extensive research on BSCF, there are

still uncertainties regarding the exact structure of the active Co/FeOOH layer, the potential synergy between Co and Fe, and the involvement of Co and/or Fe in the active site. Furthermore, it remains unclear whether this active layer forms on the BSCF support or the spinel phase. Combinational operando characterization methods offer a powerful solution by overcoming the limitations of single characterization techniques, providing a full picture of the active site. For instance, XAS is mostly adopted to determine the active Co/FeOOH layer in BSCF based on oxidation state and coordination environment. However, to establish a more convincing case, additional characterization techniques such as Raman or IR spectroscopy can be simultaneously adopted to capture the vibrational information of active site in an operando fashion.

6.3 Simulating the evolution of surface structure. Conventional computational methods, primarily DFT calculations, have been traditionally employed to calculate reaction free energies and determine the most thermodynamically favorable pathway based on a static model. The calculated surface Pourbaix diagram adds credibility to the proposed surface model. However, as discussed in section 5, the perovskite surface can undergo dynamic structural changes during operation when exposed to electrode potential and specific electrolytes, which is not included in these calculations. To address this limitation, *ab initio* molecular dynamics (AIMD) simulations offer a promising solution to simulate the surface structure evolution under a more practical condition (explicit solvent). The importance of interfacial structure (electric double-layer) between electrode and electrolyte on the reactivity can be discussed in this context[183, 184]. Recent advances in computational methods[185] allow for the simulation over significant time scales, offering valuable insights into the dynamic behavior of the perovskite surface under working conditions, though modeling complex perovskite surface needs substantial computational resources.

6.4 Establishing the activity-stability relationship. The stability of OER catalysts is a crucial aspect for industrial applications. While significant efforts have been directed previously towards enhancing the activity of catalysts by reducing overpotential, the stability of the evolved structure under working conditions, such as (oxy)hydroxide phases, remains an area requiring comprehensive research. It was observed that there is often a tradeoff between the activity and stability of OER catalysts, indicating a fundamental correlation between these two aspects[186, 187]. The surface reconstruction of perovskite oxides, induced by lattice oxygen activation, contributes to structural instability inherently through the generation of oxygen vacancies. This highlights the importance of finding unified descriptors that can dictate both the activity and stability of OER catalysts, enabling the development of balanced catalysts.

6.5 Conducting transient electrochemical measurements with spectroscopic characterization. Conventional in-situ/operando characterization conducted in steady state may inadvertently conceal crucial kinetic information or result in low coverage of active species, making it challenging to detect and analyze those using spectroscopic methods. However, transient methods such as pulse voltammetry offer a promising approach to quantitatively manipulate active species during electrochemical processes[106]. Considering the high dependence of perovskite surface reconstruction on test conditions, transient electrochemical measurements can offer an additional opportunity to quantitatively tune the evolution of surface structures using pulse excitation and directly correlate them with OER performance. Indeed, the successful integration of transient electrochemical measurements with spectroscopic characterization requires advancements in time-resolved spectroscopy techniques.

6.6 Developing surface sensitive spectroscopic techniques. Catalysis and surface reconstruction predominantly takes place on the surface of materials.

However, conventional optical spectroscopic tools like IR and Raman spectroscopy often lack surface sensitivity, providing overwhelming bulk information in most cases. While certain surface-sensitive spectroscopic techniques exist, they may be limited by the substrate used or introduce foreign materials into the system under investigation, both of which are crucial considerations in catalysis research. Additionally, some of these techniques suffer from low signal intensity or high requirement of instrumental setup. Therefore, it is imperative to develop surface-sensitive spectroscopic techniques specifically tailored for catalysis research.

Notes

The authors declare no competing financial interest.

ACKNOWLEDGMENTS

The authors gratefully acknowledge the National Natural Science Foundation of China (grants no. 22173058 and 22279077), and the Natural Science Foundation of Shanghai (22ZR1424500).

References

[1] S. Chu, A. Majumdar, Opportunities and Challenges for a Sustainable Energy Future, Nature, 2012, 488, 294-303.

[2] J. Liu, H. Mooney, V. Hull, S.J. Davis, J. Gaskell, T. Hertel, J. Lubchenco, K.C. Seto, P. Gleick, C. Kremen, S. Li, Systems Integration for Global Sustainability, Science, 2015, 347, 1258832.

[3] Q. Wang, K. Domen, Particulate Photocatalysts for Light-Driven Water Splitting: Mechanisms, Challenges, and Design Strategies, Chem. Rev., 2020, 120, 919-985.

[4] B.M. Hunter, H.B. Gray, A.M. Muller, Earth-Abundant Heterogeneous Water Oxidation Catalysts, Chem. Rev., 2016, 116, 14120-14136.

[5] D. Li, E.J. Park, W. Zhu, Q. Shi, Y. Zhou, H. Tian, Y. Lin, A. Serov, B. Zulevi, E.D. Baca, C. Fujimoto, H.T. Chung, Y.S. Kim, Highly Quaternized Polystyrene Ionomers

for High Performance Anion Exchange Membrane Water Electrolysers, Nat. Energy, 2020, 5, 378-385.

[6] S. Zuo, Z.-P. Wu, H. Zhang, X.W. Lou, Operando Monitoring and Deciphering the Structural Evolution in Oxygen Evolution Electrocatalysis, Adv. Energy Mater., 2022, 12, 2103383.

[7] F. Zeng, C. Mebrahtu, L. Liao, A.K. Beine, R. Palkovits, Stability and Deactivation of OER Electrocatalysts: A Review, J. Energy Chem., 2022, 69, 301-329.

[8] S. Chen, L. Ma, Z. Huang, G. Liang, C. Zhi, In Situ/Operando Analysis of Surface Reconstruction of Transition Metal-Based Oxygen Evolution Electrocatalysts, Cell Rep. Phys. Sci., 2022, 3, 100729.

[9] M. Chatenet, B.G. Pollet, D.R. Dekel, F. Dionigi, J. Deseure, P. Millet, R.D. Braatz, M.Z. Bazant, M. Eikerling, I. Staffell, P. Balcombe, Y. Shao-Horn, H. Schäfer, Water Electrolysis: From Textbook Knowledge to the Latest Scientific Strategies and Industrial Developments, Chem. Soc. Rev., 2022, 51, 4583-4762.

[10] N. Zhang, Y. Chai, Lattice Oxygen Redox Chemistry in Solid-State Electrocatalysts for Water Oxidation, Energy Environ. Sci., 2021, 14, 4647-4671.

[11] Z. Kou, X. Li, L. Zhang, W. Zang, X. Gao, J. Wang, Dynamic Surface Chemistry of Catalysts in Oxygen Evolution Reaction, Small Sci., 2021, 1, 2100011.

[12] L. Gao, X. Cui, C.D. Sewell, J. Li, Z. Lin, Recent Advances in Activating Surface Reconstruction for the High-Efficiency Oxygen Evolution Reaction, Chem. Soc. Rev., 2021, 50, 8428-8469.

[13] J. Chen, H. Chen, T. Yu, R. Li, Y. Wang, Z. Shao, S. Song, Recent Advances in the Understanding of the Surface Reconstruction of Oxygen Evolution Electrocatalysts and Materials Development, Electrochem. Energy Rev., 2021, 4, 566-600.

[14] J. Song, C. Wei, Z.F. Huang, C. Liu, L. Zeng, X. Wang, Z.J. Xu, A Review on Fundamentals for Designing Oxygen Evolution Electrocatalysts, Chem. Soc. Rev., 2020, 49, 2196-2214.

[15] N.T. Suen, S.F. Hung, Q. Quan, N. Zhang, Y.J. Xu, H.M. Chen, Electrocatalysis for the Oxygen Evolution Reaction: Recent Development and Future Perspectives, Chem. Soc. Rev., 2017, 46, 337-365.

[16] J. Hwang, R.R. Rao, L. Giordano, Y. Katayama, Y. Yu, Y. Shao-Horn, Perovskites in Catalysis and Electrocatalysis, Science, 2017, 358, 751-756.

[17] D.B. Meadowcroft, Low-Cost Oxygen Electrode Material, Nature, 1970, 226, 847-848.

[18] J.O.M. Bockris, T. Otagawa, Mechanism of Oxygen Evolution on Perovskites, The Journal of Physical Chemistry, 1983, 87, 2960-2971.

[19] J.O.M. Bockris, T. Otagawa, The Electrocatalysis of Oxygen Evolution on Perovskites, J. Electrochem. Soc., 1984, 131, 290-302.

[20] J. Suntivich, K.J. May, H.A. Gasteiger, J.B. Goodenough, Y. Shao-Horn, A Perovskite Oxide Optimized for Oxygen Evolution Catalysis from Molecular Orbital Principles, Science, 2011, 334, 1383-1385.

[21] K.J. May, C.E. Carlton, K.A. Stoerzinger, M. Risch, J. Suntivich, Y.L. Lee, A. Grimaud, Y. Shao-Horn, Influence of Oxygen Evolution During Water Oxidation on the Surface of Perovskite Oxide Catalysts, J. Phys. Chem. Lett., 2012, 3, 3264-3270.

[22] M. Risch, A. Grimaud, K.J. May, K.A. Stoerzinger, T.J. Chen, A.N. Mansour, Y. Shao-Horn, Structural Changes of Cobalt-Based Perovskites Upon Water Oxidation Investigated by Exafs, J. Phys. Chem. C, 2013, 117, 8628-8635.

[23] H. Jiang, Q. He, Y. Zhang, L. Song, Structural Self-Reconstruction of Catalysts in Electrocatalysis, Acc. Chem. Res., 2018, 51, 2968-2977.

[24] N. Zhang, X. Feng, D. Rao, X. Deng, L. Cai, B. Qiu, R. Long, Y. Xiong, Y. Lu, Y. Chai, Lattice Oxygen Activation Enabled by High-Valence Metal Sites for Enhanced Water Oxidation, Nat. Commun., 2020, 11, 4066.

[25] B. Zhang, K. Jiang, H. Wang, S. Hu, Fluoride-Induced Dynamic Surface Self-Reconstruction Produces Unexpectedly Efficient Oxygen-Evolution Catalyst, Nano Lett., 2019, 19, 530-537.

[26] D. Guan, G. Ryu, Z. Hu, J. Zhou, C.L. Dong, Y.C. Huang, K. Zhang, Y. Zhong, A.C. Komarek, M. Zhu, X. Wu, C.W. Pao, C.K. Chang, H.J. Lin, C.T. Chen, W. Zhou, Z. Shao, Utilizing Ion Leaching Effects for Achieving High Oxygen-Evolving Performance on Hybrid Nanocomposite with Self-Optimized Behaviors, Nat. Commun., 2020, 11, 3376.

[27] Y. Zhou, N. López, The Role of Fe Species on Niooh in Oxygen Evolution Reactions, ACS Catal., 2020, 10, 6254-6261.

[28] K. Zhu, X. Zhu, W. Yang, Application of in Situ Techniques for the Characterization of Nife-Based Oxygen Evolution Reaction (OER) Electrocatalysts, Angew. Chem. Int. Ed., 2019, 58, 1252-1265.

[29] J.H.K. Pfisterer, Y. Liang, O. Schneider, A.S. Bandarenka, Direct Instrumental Identification of Catalytically Active Surface Sites, Nature, 2017, 549, 74-77.

[30] Y. Deng, B.S. Yeo, Characterization of Electrocatalytic Water Splitting and CO_2 Reduction Reactions Using in Situ/Operando Raman Spectroscopy, ACS Catal., 2017, 7, 7873-7889.

[31] Y. Zhu, J. Wang, H. Chu, Y.-C. Chu, H.M. Chen, In Situ/Operando Studies for Designing Next-Generation Electrocatalysts, ACS Energy Lett., 2020, 5, 1281-1291.

[32] S. Song, J. Zhou, X. Su, Y. Wang, J. Li, L. Zhang, G. Xiao, C. Guan, R. Liu, S. Chen, H.-J. Lin, S. Zhang, J.-Q. Wang, Operando X-Ray Spectroscopic Tracking of Self-Reconstruction for Anchored Nanoparticles as High-Performance Electrocatalysts Towards Oxygen Evolution, Energy Environ. Sci., 2018, 11, 2945-2953.

[33] Y. Sun, R. Li, X. Chen, J. Wu, Y. Xie, X. Wang, K. Ma, L. Wang, Z. Zhang, Q. Liao, Z. Kang, Y. Zhang, A-Site Management Prompts the Dynamic Reconstructed Active Phase of Perovskite Oxide OER Catalysts, Adv. Energy Mater., 2021, 11, 2003755.

[34] J. Rossmeisl, A. Logadottir, J.K. Norskov, Electrolysis of Water on (Oxidized) Metal Surfaces, Chem. Phys., 2005, 319, 178-184.

[35] J. Rossmeisl, Z.W. Qu, H. Zhu, G.J. Kroes, J.K. Norskov, Electrolysis of Water on Oxide Surfaces, J. Electroanal. Chem., 2007, 607, 83-89.

[36] A. Grimaud, O. Diaz-Morales, B. Han, W.T. Hong, Y.L. Lee, L. Giordano, K.A. Stoerzinger, M.T.M. Koper, Y. Shao-Horn, Activating Lattice Oxygen Redox Reactions in Metal Oxides to Catalyse Oxygen Evolution, Nat. Chem., 2017, 9, 457-465.

[37] J.S. Yoo, X. Rong, Y. Liu, A.M. Kolpak, Role of Lattice Oxygen Participation in Understanding Trends in the Oxygen Evolution Reaction on Perovskites, ACS Catal., 2018, 8, 4628-4636.

[38] P. Liao, J.A. Keith, E.A. Carter, Water Oxidation on Pure and Doped Hematite (0001) Surfaces: Prediction of Co and Ni as Effective Dopants for Electrocatalysis, J. Am. Chem. Soc., 2012, 134, 13296-13309.

[39] F.-Y. Chen, Z.-Y. Wu, Z. Adler, H. Wang, Stability Challenges of Electrocatalytic Oxygen Evolution Reaction: From Mechanistic Understanding to Reactor Design, Joule, 2021, 5, 1704-1731.

[40] X. Rong, J. Parolin, A.M. Kolpak, A Fundamental Relationship between Reaction Mechanism and Stability in Metal Oxide Catalysts for Oxygen Evolution, ACS Catal., 2016, 6, 1153-1158.

[41] J.K. Norskov, J. Rossmeisl, A. Logadottir, L. Lindqvist, J.R. Kitchin, T. Bligaard, H. Jonsson, Origin of the Overpotential for Oxygen Reduction at a Fuel-Cell Cathode, J. Phys. Chem. B, 2004, 108, 17886-17892.

[42] I.C. Man, H.Y. Su, F. Calle-Vallejo, H.A. Hansen, J.I. Martínez, N.G. Inoglu, J. Kitchin, T.F. Jaramillo, J.K. Nørskov, J. Rossmeisl, Universality in Oxygen Evolution Electrocatalysis on Oxide Surfaces, ChemCatChem, 2011, 3, 1159-1165.

[43] M.T.M. Koper, Thermodynamic Theory of Multi-Electron Transfer Reactions: Implications for Electrocatalysis, J. Electroanal. Chem., 2011, 660, 254-260.

[44] H. Ooka, J. Huang, K.S. Exner, The Sabatier Principle in Electrocatalysis: Basics, Limitations, and Extensions, Front. Energy Res., 2021, 9, 654460.

[45] M.T.M. Koper, Theory of Multiple Proton–Electron Transfer Reactions and Its Implications for Electrocatalysis, Chem. Sci., 2013, 4, 2710-2723.

[46] O. Diaz-Morales, D. Ferrus-Suspedra, M.T.M. Koper, The Importance of Nickel Oxyhydroxide Deprotonation on Its Activity Towards Electrochemical Water Oxidation, Chem. Sci., 2016, 7, 2639-2645.

[47] A. Yamaguchi, R. Inuzuka, T. Takashima, T. Hayashi, K. Hashimoto, R. Nakamura, Regulating Proton-Coupled Electron Transfer for Efficient Water Splitting by Manganese Oxides at Neutral Ph, Nat. Commun., 2014, 5, 4256.

[48] J.K. Norskov, T. Bligaard, A. Logadottir, S. Bahn, L.B. Hansen, M. Bollinger, H. Bengaard, B. Hammer, Z. Sljivancanin, M. Mavrikakis, Y. Xu, S. Dahl, C.J.H. Jacobsen, Universality in Heterogeneous Catalysis, J. Catal., 2002, 209, 275-278.

[49] P. Steegstra, M. Busch, I. Panas, E. Ahlberg, Revisiting the Redox Properties of Hydrous Iridium Oxide Films in the Context of Oxygen Evolution, J. Phys. Chem. C, 2013, 117, 20975-20981.

[50] M. Busch, E. Ahlberg, I. Panas, Water Oxidation on Mno_x and Iro_x: Why Similar Performance?, J. Phys. Chem. C, 2012, 117, 288-292.

[51] H. Ooka, Y. Wang, A. Yamaguchi, M. Hatakeyama, S. Nakamura, K. Hashimoto, R. Nakamura, Legitimate Intermediates of Oxygen Evolution on Iridium Oxide Revealed by in Situ Electrochemical Evanescent Wave Spectroscopy, Phys. Chem. Chem. Phys., 2016, 18, 15199-15204.

[52] G.M. Tomboc, S. Venkateshalu, Q.-T. Ngo, S. Choi, B.G. Pollet, H. Lee, K. Lee, Defect-Induced Electronic Modification and Surface Reconstruction of Catalysts During Water Oxidation Process, Chem. Eng. J., 2023, 454, 140254.

[53] J.-P. Tessonnier, D. Rosenthal, T.W. Hansen, C. Hess, M.E. Schuster, R. Blume, F. Girgsdies, N. Pfaender, O. Timpe, D.S. Su, R. Schloegl, Analysis of the Structure and Chemical Properties of Some Commercial Carbon Nanostructures, Carbon, 2009, 47, 1779-1798.

[54] K. Macounova, M. Makarova, P. Krtil, Oxygen Evolution on Nanocrystalline RuO_2 and $Ru_{0.9}Ni_{0.1}O_{2-\delta}$ Electrodes–Dems Approach to Reaction Mechanism Determination, Electrochem. Commun., 2009, 11, 1865-1868.

[55] W.-M. M, H. J, Oxygen Evolution on Ru and Ruo_2 Electrodes Studied Using Isotope Labelling and on-Line Mass Spectrometry J. Electroanal. Chem. Interfacial Electrochem., 1987, 237, 251-260.

[56] S. Fierro, T. Nagel, H. Baltruschat, C. Comninellis, Investigation of the Oxygen Evolution Reaction on Ti/Iro_2 Electrodes Using Isotope Labelling and on-Line Mass Spectrometry, Electrochem. Commun., 2007, 9, 1969-1974.

[57] K. Schweinar, B. Gault, I. Mouton, O. Kasian, Lattice Oxygen Exchange in Rutile Iro_2 During the Oxygen Evolution Reaction, J Phys. Chem. Lett., 2020, 11, 5008-5014.

[58] B. Han, A. Grimaud, L. Giordano, W.T. Hong, O. Diaz-Morales, L. Yueh-Lin, J. Hwang, N. Charles, K.A. Stoerzinger, W. Yang, M.T.M. Koper, Y. Shao-Horn, Iron-Based Perovskites for Catalyzing Oxygen Evolution Reaction, J. Phys. Chem. C, 2018,

122, 8445-8454.

[59] K.A. Stoerzinger, O. Diaz-Morales, M. Kolb, R.R. Rao, R. Frydendal, L. Qiao, X.R. Wang, N.B. Halck, J. Rossmeisl, H.A. Hansen, T. Vegge, I.E.L. Stephens, M.T.M. Koper, Y. Shao-Horn, Orientation-Dependent Oxygen Evolution on RuO_2 without Lattice Exchange, ACS Energy Lett., 2017, 2, 876-881.

[60] S.B. Scott, J.E. Sørensen, R.R. Rao, C. Moon, J. Kibsgaard, Y. Shao-Horn, I. Chorkendorff, The Low Overpotential Regime of Acidic Water Oxidation Part II: Trends in Metal and Oxygen Stability Numbers, Energy Environ. Sci., 2022, 15, 1988-2001.

[61] J.T. Mefford, X. Rong, A.M. Abakumov, W.G. Hardin, S. Dai, A.M. Kolpak, K.P. Johnston, K.J. Stevenson, Water Electrolysis on $La_{1-x}Sr_xCoO_{3-\delta}$ Perovskite Electrocatalysts, Nat Commun, 2016, 7, 11053.

[62] W.G. Hardin, J.T. Mefford, D.A. Slanac, B.B. Patel, X. Wang, S. Dai, X. Zhao, R.S. Ruoff, K.P. Johnston, K.J. Stevenson, Tuning the Electrocatalytic Activity of Perovskites through Active Site Variation and Support Interactions, Chem. Mater., 2014, 26, 3368-3376.

[63] W.G. Hardin, D.A. Slanac, X. Wang, S. Dai, K.P. Johnston, K.J. Stevenson, Highly Active, Nonprecious Metal Perovskite Electrocatalysts for Bifunctional Metal-Air Battery Electrodes, J. Phys. Chem. Lett., 2013, 4, 1254-1259.

[64] X. Rong, A.M. Kolpak, Ab Initio Approach for Prediction of Oxide Surface Structure, Stoichiometry, and Electrocatalytic Activity in Aqueous Solution, J. Phys. Chem. Lett., 2015, 6, 1785-1789.

[65] T. Binninger, R. Mohamed, K. Waltar, E. Fabbri, P. Levecque, R. Kotz, T.J. Schmidt, Thermodynamic Explanation of the Universal Correlation between Oxygen Evolution Activity and Corrosion of Oxide Catalysts, Sci Rep, 2015, 5, 12167.

[66] S.C.W. Zhaoning Song, Adam B. Phillips, Michael J. Heben, Pathways toward High-Performance Perovskite Solar Cells: Review of Recent Advances in Organo-Metal Halide Perovskites for Photovoltaic Applications, J. Photon. Energy, 2016, 6, 022001.

[67] D. Liu, P. Zhou, H. Bai, H. Ai, X. Du, M. Chen, D. Liu, W.F. Ip, K.H. Lo, C.T.

Kwok, S. Chen, S. Wang, G. Xing, X. Wang, H. Pan, Development of Perovskite Oxide-Based Electrocatalysts for Oxygen Evolution Reaction, Small, 2021, e2101605.

[68] J. Zhu, H. Li, L. Zhong, P. Xiao, X. Xu, X. Yang, Z. Zhao, J. Li, Perovskite Oxides: Preparation, Characterizations, and Applications in Heterogeneous Catalysis, ACS Catal., 2014, 4, 2917-2940.

[69] S. Royer, D. Duprez, F. Can, X. Courtois, C. Batiot-Dupeyrat, S. Laassiri, H. Alamdari, Perovskites as Substitutes of Noble Metals for Heterogeneous Catalysis: Dream or Reality, Chem. Rev., 2014, 114, 10292-10368.

[70] A.M. Glazer, Simple Ways of Determining Perovskite Structures, Acta Cryst., 1975, 31, 756-762.

[71] V.M. Goldschmidt, Die Gesetze Der Krystallochemie, Naturwissenschaften, 1926, 14, 477-485.

[72] Xiao Liang, Ke-Xin Zhang, Yu-Cheng Shen, L.S. Ke Sun, Hui Chen, Ke-Yan Zheng, X.-X. Zou, Perovskite-Type Water Oxidation Electrocatalysts, J. Electrochem. , 2022, 28, 2214004.

[73] C.J. Bartel, C. Sutton, B.R. Goldsmith, R. Ouyang, C.B. Musgrave, L.M. Ghiringhelli, M. Scheffler, New Tolerance Factor to Predict the Stability of Perovskite Oxides and Halides, Sci. Adv., 2019, 5, eaav0693.

[74] X. Xu, W. Wang, W. Zhou, Z. Shao, Recent Advances in Novel Nanostructuring Methods of Perovskite Electrocatalysts for Energy-Related Applications, Small Methods, 2018, 2, 1800071.

[75] M.A. Peña, J.L.G. Fierro, Chemical Structures and Performance of Perovskite Oxides, Chem. Rev., 2001, 101, 1981-2018.

[76] Y. Zhu, W. Zhou, Z.G. Chen, Y. Chen, C. Su, M.O. Tade, Z. Shao, $SrNb_{0.1}Co_{0.7}Fe_{0.2}O_{3-\delta}$ Perovskite as a Next-Generation Electrocatalyst for Oxygen Evolution in Alkaline Solution, Angew. Chem. Int. Ed., 2015, 54, 3897-3901.

[77] A.I. Becerro, F. Langenhorst, R.J. Angel, S. Marion, C.A. McCammon, F. Seifert, The Transition from Short-Range to Long-Range Ordering of Oxygen Vacancies in $CaFe_xTi_{1-X}O_{3-X/2}$ Perovskites, Phys. Chem. Chem. Phys., 2000, 2, 3933-3941.

[78] C. Bloed, J. Vuong, A. Enriquez, S. Raghavan, I. Tran, S. Derakhshan, H. Tavassol,

Oxygen Vacancy and Chemical Ordering Control Oxygen Evolution Activity of $Sr_{2-x}Ca_xFe_2O_{6-\delta}$ Perovskites, ACS Appl. Energy Mater., 2019, 2, 6140-6145.

[79] J. Sun, L. Du, B. Sun, G. Han, Y. Ma, J. Wang, H. Huo, C. Du, G. Yin, Bifunctional $LaMn_{0.3}Co_{0.7}O_3$ Perovskite Oxide Catalyst for Oxygen Reduction and Evolution Reactions: The Optimized Eg Electronic Structures by Manganese Dopant, ACS Appl. Mater. Interfaces, 2020, 12, 24717-24725.

[80] J. Yu, D. Chen, M. Saccoccio, K. Lam, F. Ciucci, Promotion of Oxygen Reduction with Both Amorphous and Crystalline Mno_x through the Surface Engineering of $La_{0.8}sr_{0.2}mno_{3-\Delta}$ Perovskite, ChemElectroChem, 2018, 5, 1105-1112.

[81] B. Weng, Z. Song, R. Zhu, Q. Yan, Q. Sun, C.G. Grice, Y. Yan, W.J. Yin, Simple Descriptor Derived from Symbolic Regression Accelerating the Discovery of New Perovskite Catalysts, Nat. Commun., 2020, 11, 3513.

[82] G. Koch, M. Hävecker, D. Teschner, S.J. Carey, Y. Wang, P. Kube, W. Hetaba, T. Lunkenbein, G. Auffermann, O. Timpe, F. Rosowski, R. Schlögl, A. Trunschke, Surface Conditions That Constrain Alkane Oxidation on Perovskites, ACS Catal., 2020, 10, 7007-7020.

[83] A. Trunschke, G. Bellini, M. Boniface, S.J. Carey, J. Dong, E. Erdem, L. Foppa, W. Frandsen, M. Geske, L.M. Ghiringhelli, F. Girgsdies, R. Hanna, M. Hashagen, M. Haevecker, G. Huff, A. Knop-Gericke, G. Koch, P. Kraus, J. Kroehnert, P. Kube, S. Lohr, T. Lunkenbein, L. Masliuk, R.N. d'Alnoncourt, T. Omojola, C. Pratsch, S. Richter, C. Rohner, F. Rosowski, F. Ruether, M. Scheffler, R. Schloegl, A. Tarasov, D. Teschner, O. Timpe, P. Trunschke, Y. Wang, S. Wrabetz, Towards Experimental Handbooks in Catalysis, Top. Catal., 2020, 63, 1683-1699.

[84] L. C., Seitz, C. F., Dickens, Kazunori Nishio, Yasuyuki Hikita, Joseph Montoya, Andrew Doyle, Charlotte Kirk, Aleksandra Vojvodic, Harold Y. Hwang, Jens K. Norskov, T.F. Jaramillo, A Highly Active and Stable $Iro_x/Sriro_3$ Catalyst for the Oxygen Evolution Reaction, Science, 2016, 353, 1011-1014.

[85] R. Polini, A. Pamio, E. Traversa, Effect of Synthetic Route on Sintering Behaviour, Phase Purity and Conductivity of Sr- and Mg-Doped $LaGaO_3$ Perovskites, J. Eur. Ceram. Soc., 2004, 24, 1365-1370.

[86] H. Xia, J. Dai, Y. Xu, Y. Yin, X. Wang, Z. Liu, M. Liu, M.A. McGuire, X. Li, Z. Li, C. Jin, Y. Yang, J. Zhou, Y. Long, Magnetism and the Spin State in Cubic Perovskite $CaCoO_3$ Synthesized under High Pressure, Phys. Rev. Mater., 2017, 1, 024406.

[87] L. Tang, W. Zhang, D. Lin, Y. Ren, H. Zheng, Q. Luo, L. Wei, H. Liu, J. Chen, K. Tang, The Hexagonal Perovskite $Ba_{0.5}Sr_{0.5}Co_{0.8}Fe_{0.2}O_{3-\delta}$ as an Efficient Electrocatalyst for the Oxygen Evolution Reaction, Inorg. Chem. Front., 2020, 7, 4488-4497.

[88] Y. Matsumoto, S. Yamada, T. Nishida, E. Sato, Oxygen Evolution on $La_{1-X}Sr_xFe_{1-Y}Co_YO_3$ Series Oxides, J. Electrochem. Soc., 1980, 127, 2360-2364.

[89] M. Bursell, M. Pirjamali, Y. Kiros, $La_{0.6}Ca_{0.4}CoO_3$, $La_{0.1}Ca_{0.9}MnO_3$ and $LaNiO_3$ Oxygen Electrodes, Electrochim. Acta, 2002, 47, 1651-1660.

[90] J. Kim, X. Yin, K.C. Tsao, S. Fang, H. Yang, $Ca_2Mn_2O_5$ as Oxygen-Deficient Perovskite Electrocatalyst for Oxygen Evolution Reaction, J. Am. Chem. Soc., 2014, 136, 14646-14649.

[91] Y. Tong, Y. Guo, P. Chen, H. Liu, M. Zhang, L. Zhang, W. Yan, W. Chu, C. Wu, Y. Xie, Spin-State Regulation of Perovskite Cobaltite to Realize Enhanced Oxygen Evolution Activity, Chem, 2017, 3, 812-821.

[92] A. Grimaud, K.J. May, C.E. Carlton, Y.L. Lee, M. Risch, W.T. Hong, J. Zhou, Y. Shao-Horn, Double Perovskites as a Family of Highly Active Catalysts for Oxygen Evolution in Alkaline Solution, Nat. Commun., 2013, 4, 2439.

[93] W.T. Hong, K.A. Stoerzinger, Y.L. Lee, L. Giordano, A. Grimaud, A.M. Johnson, J. Hwang, E.J. Crumlin, W.L. Yang, Y. Shao-Horn, Charge-Transfer-Energy-Dependent Oxygen Evolution Reaction Mechanisms for Perovskite Oxides, Energy Environ. Sci., 2017, 10, 2190-2200.

[94] W.T. Hong, M. Risch, K.A. Stoerzinger, A. Grimaud, J. Suntivich, Y. Shao-Horn, Toward the Rational Design of Non-Precious Transition Metal Oxides for Oxygen Electrocatalysis, Energy Environ. Sci., 2015, 8, 1404-1427.

[95] I. Yamada, A. Takamatsu, K. Asai, T. Shirakawa, H. Ohzuku, A. Seno, T. Uchimura, H. Fujii, S. Kawaguchi, K. Wada, H. Ikeno, S. Yagi, Systematic Study of Descriptors for Oxygen Evolution Reaction Catalysis in Perovskite Oxides, J. Phys. Chem. C, 2018, 122, 27885-27892.

[96] M. Arnold, T.M. Gesing, J. Martynczuk, A. Feldhoff, Correlation of the Formation and the Decomposition Process of the Bscf Perovskite at Intermediate Temperatures, Chem. Mater., 2008, 20, 5851-5858.

[97] K. Ma, Y. Zhang, L. Liu, J. Xi, X. Qiu, T. Guan, Y. He, In Situ Mapping of Activity Distribution and Oxygen Evolution Reaction in Vanadium Flow Batteries, Nat Commun, 2019, 10, 5286.

[98] T.A. Nijhuis, S.J. Tinnemans, T. Visser, B.M. Weckhuysen, Operando Spectroscopic Investigation of Supported Metal Oxide Catalysts by Combined Time-Resolved UV-Vis/Raman/on-Line Mass Spectrometry, Phys. Chem. Chem. Phys., 2003, 5, 4361-4365.

[99] J. Li, J. Gong, Operando Characterization Techniques for Electrocatalysis, Energy Environ. Sci., 2020, 13, 3748-3779.

[100] N. Ortiz Pena, D. Ihiawakrim, M. Han, B. Lassalle-Kaiser, S. Carenco, C. Sanchez, C. Laberty-Robert, D. Portehault, O. Ersen, Morphological and Structural Evolution of Co_3O_4 Nanoparticles Revealed by in Situ Electrochemical Transmission Electron Microscopy During Electrocatalytic Water Oxidation, ACS Nano, 2019, 13, 11372-11381.

[101] T. Binninger, E. Fabbri, A. Patru, M. Garganourakis, J. Han, D.F. Abbott, O. Sereda, R. Kötz, A. Menzel, M. Nachtegaal, T.J. Schmidt, Electrochemical Flow-Cell Setup for in Situ X-Ray Investigations, J. Electrochem. Soc., 2016, 163, H906-H912.

[102] V. Streibel, M. Hävecker, Y. Yi, J.J. Velasco Vélez, K. Skorupska, E. Stotz, A. Knop-Gericke, R. Schlögl, R. Arrigo, In Situ Electrochemical Cells to Study the Oxygen Evolution Reaction by near Ambient Pressure X-Ray Photoelectron Spectroscopy, Top. Catal., 2018, 61, 2064-2084.

[103] W.H. Lee, M.H. Han, Y.J. Ko, B.K. Min, K.H. Chae, H.S. Oh, Electrode Reconstruction Strategy for Oxygen Evolution Reaction: Maintaining Fe-Coooh Phase with Intermediate-Spin State During Electrolysis, Nat. Commun., 2022, 13, 605.

[104] I.S. Filimonenkov, S.Y. Istomin, E.V. Antipov, G.A. Tsirlina, E.R. Savinova, Rotating Ring-Disk Electrode as a Quantitative Tool for the Investigation of the Oxygen Evolution Reaction, Electrochim. Acta, 2018, 286, 304-312.

[105] B. You, N. Jiang, M. Sheng, M.W. Bhushan, Y. Sun, Hierarchically Porous Urchin-Like Ni2p Superstructures Supported on Nickel Foam as Efficient Bifunctional Electrocatalysts for Overall Water Splitting, ACS Catal., 2015, 6, 714-721.

[106] J. Timoshenko, A. Bergmann, C. Rettenmaier, A. Herzog, R.M. Arán-Ais, H.S. Jeon, F.T. Haase, U. Hejral, P. Grosse, S. Kühl, E.M. Davis, J. Tian, O. Magnussen, B. Roldan Cuenya, Steering the Structure and Selectivity of CO_2 Electroreduction Catalysts by Potential Pulses, Nat. Catal., 2022, 5, 259-267.

[107] S. Anantharaj, S. Noda, Appropriate Use of Electrochemical Impedance Spectroscopy in Water Splitting Electrocatalysis, Chemelectrochem, 2020, 7, 2297-2308.

[108] Y. Lu, W. Wang, F. Xie, Investigation of Oxygen Evolution Reaction Kinetic Process and Kinetic Parameters on Iridium Electrode by Electrochemistry Impedance Spectroscopy Analysis, J. Electroanal. Chem., 2020, 871, 114281.

[109] A.R.C. Bredar, A.L. Chown, A.R. Burton, B.H. Farnum, Electrochemical Impedance Spectroscopy of Metal Oxide Electrodes for Energy Applications, ACS Appl. Energy Mater., 2020, 3, 66-98.

[110] D. Liu, Z. Shadike, R. Lin, K. Qian, H. Li, K. Li, S. Wang, Q. Yu, M. Liu, S. Ganapathy, X. Qin, Q.H. Yang, M. Wagemaker, F. Kang, X.Q. Yang, B. Li, Review of Recent Development of in Situ/Operando Characterization Techniques for Lithium Battery Research, Adv. Mater., 2019, 31, e1806620.

[111] D.F. Parsons, Structure of Wet Specimens in Electron Microscopy, Science, 1974, 186, 407-414.

[112] J. Timoshenko, B.R. Cuenya, In Situ/Operando Electrocatalyst Characterization by X-Ray Absorption Spectroscopy, Chem. Rev., 2021, 121, 882-961.

[113] F. Frati, M.O.J.Y. Hunault, F.M.F. de Groot, Oxygen K-Edge X-Ray Absorption Spectra, Chem. Rev., 2020, 120, 4056-4110.

[114] G. Bunker, Introduction to Xafs: A Practical Guide to X-Ray Absorption Fine Structure Spectroscopy, Cambridge University Press, Cambridge, 2010.

[115] H. Sun, W. Zhou, Progress on X-Ray Absorption Spectroscopy for the Characterization of Perovskite-Type Oxide Electrocatalysts, Energy & Fuels, 2021, 35,

5716-5737.

[116] A. Knop-Gericke, E. Kleimenov, M. Hävecker, R. Blume, D. Teschner, S. Zafeiratos, R. Schlögl, V.I. Bukhtiyarov, V.V. Kaichev, I.P. Prosvirin, A.I. Nizovskii, H. Bluhm, A. Barinov, P. Dudin, M. Kiskinova, Chapter 4 X-Ray Photoelectron Spectroscopy for Investigation of Heterogeneous Catalytic Processes, Adv. Catal., 2009, 52, 213-272.

[117] M.P. Seah, W.A. Dench, Quantitative Electron Spectroscopy of Surfaces: A Standard Data Base for Electron Inelastic Mean Free Paths in Solids, Surf. Interface Anal., 1979, 1, 2-11.

[118] D. Frank Ogletree, H. Bluhm, E.D. Hebenstreit, M. Salmeron, Photoelectron Spectroscopy under Ambient Pressure and Temperature Conditions, Nucl. Instrum. Methods Phys. Res., Sect. A, 2009, 601, 151-160.

[119] P. Amann, D. Degerman, M.-T. Lee, J.D. Alexander, M. Shipilin, H.-Y. Wang, F. Cavalca, M. Weston, J. Gladh, M. Blom, M. Björkhage, P. Löfgren, C. Schlueter, P. Loemker, K. Ederer, W. Drube, H. Noei, J. Zehetner, H. Wentzel, J. Åhlund, A. Nilsson, A High-Pressure X-Ray Photoelectron Spectroscopy Instrument for Studies of Industrially Relevant Catalytic Reactions at Pressures of Several Bars, Rev. Sci. Instrum., 2019, 90, 103102.

[120] R. Arrigo, M. Hävecker, M.E. Schuster, C. Ranjan, E. Stotz, A. Knop-Gericke, R. Schlögl, In Situ Study of the Gas-Phase Electrolysis of Water on Platinum by Nap-Xps, Angew. Chem. Int. Ed., 2013, 52, 11660-11664.

[121] V. Pfeifer, T.E. Jones, J.J. Velasco Vélez, R. Arrigo, S. Piccinin, M. Hävecker, A. Knop-Gericke, R. Schlögl, In Situ Observation of Reactive Oxygen Species Forming on Oxygen-Evolving Iridium Surfaces, Chem. Sci., 2017, 8, 2143-2149.

[122] Z. Wu, Q. Gan, X. Li, Y. Zhong, H. Wang, Elucidating Surface Restructuring-Induced Catalytic Reactivity of Cobalt Phosphide Nanoparticles under Electrochemical Conditions, J. Phys. Chem. C, 2018, 122, 2848-2853.

[123] P. Stair, The Application of Uv Raman Spectroscopy for the Characterization of Catalysts and Catalytic Reactions, Adv. Catal., 2007, 51, 75-98.

[124] C. Hess, New Advances in Using Raman Spectroscopy for the Characterization

of Catalysts and Catalytic Reactions, Chem. Soc. Rev., 2021, 50, 3519-3564.

[125] O. Masatoshi, Dynamic Processes in Electrochemical Reactions Studied by Surface-Enhanced Infrared Absorption Spectroscopy (SEIRAS), Bull. Chem. Soc. Jpn., 1997, 70, 2861-2880.

[126] M. Fleischmann, P.J. Hendra, A.J. McQuillan, Raman Spectra of Pyridine Adsorbed at a Silver Electrode, Chem. Phys. Lett., 1974, 26, 163-166.

[127] M.-h. Shao, P. Liu, R.R. Adzic, Superoxide Anion Is the Intermediate in the Oxygen Reduction Reaction on Platinum Electrodes, J. Am. Chem. Soc., 2006, 128, 7408-7409.

[128] S. Kukunuri, H. Noguchi, In Situ Spectroscopy Study of Oxygen Reduction Reaction Intermediates at the Pt/Acid Interface: Surface-Enhanced Infrared Absorbance Spectroscopy, J. Phys. Chem. C, 2020, 124, 7267-7273.

[129] W.H. Lee, M.H. Han, Y.-J. Ko, B.K. Min, K.H. Chae, H.-S. Oh, Electrode Reconstruction Strategy for Oxygen Evolution Reaction: Maintaining Fe-Coooh Phase with Intermediate-Spin State During Electrolysis, Nat. Commun., 2022, 13, 605.

[130] B.S. Yeo, A.T. Bell, Enhanced Activity of Gold-Supported Cobalt Oxide for the Electrochemical Evolution of Oxygen, J. Am. Chem. Soc., 2011, 133, 5587-5593.

[131] B.J. Trześniewski, O. Diaz-Morales, D.A. Vermaas, A. Longo, W. Bras, M.T.M. Koper, W.A. Smith, In Situ Observation of Active Oxygen Species in Fe-Containing Ni-Based Oxygen Evolution Catalysts: The Effect of Ph on Electrochemical Activity, J. Am. Chem. Soc., 2015, 137, 15112-15121.

[132] S. Zerebecki, S. Salamon, J. Landers, Y. Yang, Y. Tong, E. Budiyanto, D. Waffel, M. Dreyer, S. Saddeler, T. Kox, S. Kenmoe, E. Spohr, S. Schulz, M. Behrens, M. Muhler, H. Tüysüz, R. Kramer Campen, H. Wende, S. Reichenberger, S. Barcikowski, Engineering of Cation Occupancy of $CoFe_2O_4$ Oxidation Catalysts by Nanosecond, Single-Pulse Laser Excitation in Water, ChemCatChem, 2022, 14, e202101785.

[133] S. Wahl, S.M. El-Refaei, P. Amsalem, A.G. Buzanich, N. Koch, N. Pinna, Operando Diffuse Reflectance Uv-Vis Spectroelectrochemistry for Investigating Oxygen Evolution Electrocatalysts, Catal. Sci. Technol., 2020, 10, 517-528.

[134] O. Mabayoje, A. Shoola, B.R. Wygant, C.B. Mullins, The Role of Anions in Metal

Chalcogenide Oxygen Evolution Catalysis: Electrodeposited Thin Films of Nickel Sulfide as “Pre-Catalysts”, ACS Energy Lett., 2016, 1, 195-201.

[135] Z. Qiu, C.-W. Tai, G.A. Niklasson, T. Edvinsson, Direct Observation of Active Catalyst Surface Phases and the Effect of Dynamic Self-Optimization in Nife-Layered Double Hydroxides for Alkaline Water Splitting, Energy Environ. Sci., 2019, 12, 572-581.

[136] C. Gu, S. Hu, X. Zheng, M.R. Gao, Y.R. Zheng, L. Shi, Q. Gao, X. Zheng, W. Chu, H.B. Yao, J. Zhu, S.H. Yu, Synthesis of Sub-2 nm Iron-Doped $NiSe_2$ Nanowires and Their Surface-Confined Oxidation for Oxygen Evolution Catalysis, Angew. Chem. Int. Ed., 2018, 57, 4020-4024.

[137] Y. Zhu, H.-C. Chen, C.-S. Hsu, T.-S. Lin, C.-J. Chang, S.-C. Chang, L.-D. Tsai, H.M. Chen, Operando Unraveling of the Structural and Chemical Stability of P-Substituted $CoSe_2$ Electrocatalysts toward Hydrogen and Oxygen Evolution Reactions in Alkaline Electrolyte, ACS Energy Lett., 2019, 4, 987-994.

[138] Y. Zhang, L. Gao, E.J.M. Hensen, J.P. Hofmann, Evaluating the Stability of Co_2p Electrocatalysts in the Hydrogen Evolution Reaction for Both Acidic and Alkaline Electrolytes, ACS Energy Lett., 2018, 3, 1360-1365.

[139] Gang Wan, John W. Freeland, Jan Kloppenburg, Guido Petretto, Jocienne N. Nelson, Ding-Yuan Kuo, Cheng-Jun Sun, Jianguo Wen, J. Trey Diulus, Gregory S. Herman, Yongqi Dong, Ronghui Kou, Jingying Sun, Shuo Chen, Kyle M. Shen, Darrell G. Schlom, Gian-Marco Rignanese, Geoffroy Hautier, Dillon D. Fong, Zhenxing Feng, J.S. Hua Zhou, Amorphization Mechanism of $SrIrO_3$ Electrocatalyst: How Oxygen Redox Initiates Ionic Diffusion and Structural Reorganization, Sci. Adv., 2021, 7, 7323.

[140] M. Ben-Naim, Y. Liu, M.B. Stevens, K. Lee, M.R. Wette, A. Boubnov, A.A. Trofimov, A.V. Ievlev, A. Belianinov, R.C. Davis, B.M. Clemens, S.R. Bare, Y. Hikita, H.Y. Hwang, D.C. Higgins, R. Sinclair, T.F. Jaramillo, Understanding Degradation Mechanisms in $Sriro_3$ Oxygen Evolution Electrocatalysts: Chemical and Structural Microscopy at the Nanoscale, Adv. Funct. Mater., 2021, 31, 2101542.

[141] C.W. Song, H. Suh, J. Bak, H.B. Bae, S.-Y. Chung, Dissolution-Induced Surface Roughening and Oxygen Evolution Electrocatalysis of Alkaline-Earth Iridates in Acid,

Chem, 2019, 5, 3243-3259.

[142] S. Samira, J. Hong, J.C.A. Camayang, K. Sun, A.S. Hoffman, S.R. Bare, E. Nikolla, Dynamic Surface Reconstruction Unifies the Electrocatalytic Oxygen Evolution Performance of Nonstoichiometric Mixed Metal Oxides, JACS Au, 2021, 1, 2224-2241.

[143] W. Jung, H.L. Tuller, Investigation of Surface Sr Segregation in Model Thin Film Solid Oxide Fuel Cell Perovskite Electrodes, Energy Environ. Sci., 2012, 5, 5370-5378.

[144] Yue Zhu, Dongdong Liu, Huijuan Jing, Fei Zhang, Xiaoben Zhang, Shiqing Hu, Liming Zhang, Jingyi Wang, Lixiao Zhang, Wenhao Zhang, Bingjie Pang, Peng Zhang, Fengtao Fan, Jianping Xiao, Wei Liu, Xuefeng Zhu, W. Yang, Oxygen Activation on Ba-Containing Perovskite Materials, Sci. Adv., 2022, 8, eabn4072.

[145] S. Geiger, O. Kasian, M. Ledendecker, E. Pizzutilo, A.M. Mingers, W.T. Fu, O. Diaz-Morales, Z. Li, T. Oellers, L. Fruchter, A. Ludwig, K.J.J. Mayrhofer, M.T.M. Koper, S. Cherevko, The Stability Number as a Metric for Electrocatalyst Stability Benchmarking, Nat. Catal., 2018, 1, 508-515.

[146] Yubo Chen, Yuanmiao Sun, Maoyu Wang, Jingxian Wang, Haiyan Li, Shibo Xi, Chao Wei, Pinxian Xi, George E. Sterbinsky, John W. Freeland, Adrian C. Fisher, Joel W. Ager III, Zhenxing Feng, Z.J. Xu, Lattice Site–Dependent Metal Leaching in Perovskites toward a Honeycomb-Like Water Oxidation Catalyst, Sci. Adv., 2021, 7, eabk1788

[147] E. Fabbri, M. Nachtegaal, T. Binninger, X. Cheng, B.J. Kim, J. Durst, F. Bozza, T. Graule, R. Schaublin, L. Wiles, M. Pertoso, N. Danilovic, K.E. Ayers, T.J. Schmidt, Dynamic Surface Self-Reconstruction Is the Key of Highly Active Perovskite Nano-Electrocatalysts for Water Splitting, Nat Mater, 2017, 16, 925-931.

[148] Y. Chen, H. Li, J. Wang, Y. Du, S. Xi, Y. Sun, M. Sherburne, J.W. Ager, 3rd, A.C. Fisher, Z.J. Xu, Exceptionally Active Iridium Evolved from a Pseudo-Cubic Perovskite for Oxygen Evolution in Acid, Nat Commun, 2019, 10, 572.

[149] B.-J. Kim, E. Fabbri, D.F. Abbott, X. Cheng, A.H. Clark, M. Nachtegaal, M. Borlaf, I.E. Castelli, T. Graule, T.J. Schmidt, Functional Role of Fe-Doping in Co-Based Perovskite Oxide Catalysts for Oxygen Evolution Reaction, J. Am. Chem. Soc., 2019,

141, 5231-5240.

[150] C. Baeumer, J. Li, Q. Lu, A.Y.-L. Liang, L. Jin, H.P. Martins, T. Duchoň, M. Glöß, S.M. Gericke, M.A. Wohlgemuth, M. Giesen, E.E. Penn, R. Dittmann, F. Gunkel, R. Waser, M. Bajdich, S. Nemšák, J.T. Mefford, W.C. Chueh, Tuning Electrochemically Driven Surface Transformation in Atomically Flat $LaNiO_3$ Thin Films for Enhanced Water Electrolysis, Nat. Mater., 2021, 20, 674-682.

[151] H. Li, S. Sun, S. Xi, Y. Chen, T. Wang, Y. Du, M. Sherburne, J.W. Ager, A.C. Fisher, Z.J. Xu, Metal–Oxygen Hybridization Determined Activity in Spinel-Based Oxygen Evolution Catalysts: A Case Study of $ZnFe_{2-X}Cr_xO_4$, Chem. Mater., 2018, 30, 6839-6848.

[152] Y. Duan, S. Sun, S. Xi, X. Ren, Y. Zhou, G. Zhang, H. Yang, Y. Du, Z.J. Xu, Tailoring the Co 3d-O 2p Covalency in Lacoo3 by Fe Substitution to Promote Oxygen Evolution Reaction, Chem. Mater., 2017, 29, 10534-10541.

[153] S. Yagi, I. Yamada, H. Tsukasaki, A. Seno, M. Murakami, H. Fujii, H. Chen, N. Umezawa, H. Abe, N. Nishiyama, S. Mori, Covalency-Reinforced Oxygen Evolution Reaction Catalyst, Nat. Commun., 2015, 6, 8249.

[154] J. Suntivich, W.T. Hong, Y.-L. Lee, J.M. Rondinelli, W. Yang, J.B. Goodenough, B. Dabrowski, J.W. Freeland, Y. Shao-Horn, Estimating Hybridization of Transition Metal and Oxygen States in Perovskites from O K-Edge X-Ray Absorption Spectroscopy, J. Phys. Chem. C, 2014, 118, 1856-1863.

[155] J.T. Mefford, X. Rong, A.M. Abakumov, W.G. Hardin, S. Dai, A.M. Kolpak, K.P. Johnston, K.J. Stevenson, Water Electrolysis on $La_{1-X}Sr_xCoO_{3-\delta}$ Perovskite Electrocatalysts, Nat. Commun., 2016, 7, 11053.

[156] S. Song, J. Zhou, J. Sun, S. Zhang, X. Lin, Z. Hu, J. Hu, L. Zhang, J.-Q. Wang, Understanding the Origin of High Oxygen Evolution Reaction Activity in the High Sr-Doped Perovskite, Chin. J. Catal., 2020, 41, 592-597.

[157] A.S. Raman, R. Patel, A. Vojvodic, Surface Stability of Perovskite Oxides under Oer Operating Conditions: A First Principles Approach, Faraday Discuss., 2021, 229, 75-88.

[158] R. Zhang, N. Dubouis, M. Ben Osman, W. Yin, M.T. Sougrati, D.A.D. Corte, D.

Giaume, A. Grimaud, A Dissolution/Precipitation Equilibrium on the Surface of Iridium-Based Perovskites Controls Their Activity as Oxygen Evolution Reaction Catalysts in Acidic Media, Angew. Chem. Int. Ed., 2019, 58, 4571-4575.

[159] B.-J. Kim, D.F. Abbott, X. Cheng, E. Fabbri, M. Nachtegaal, F. Bozza, I.E. Castelli, D. Lebedev, R. Schäublin, C. Copéret, T. Graule, N. Marzari, T.J. Schmidt, Unraveling Thermodynamics, Stability, and Oxygen Evolution Activity of Strontium Ruthenium Perovskite Oxide, ACS Catal., 2017, 7, 3245-3256.

[160] B.-J. Kim, X. Cheng, D.F. Abbott, E. Fabbri, F. Bozza, T. Graule, I.E. Castelli, L. Wiles, N. Danilovic, K.E. Ayers, N. Marzari, T.J. Schmidt, Highly Active Nanoperovskite Catalysts for Oxygen Evolution Reaction: Insights into Activity and Stability of $Ba_{0.5}Sr_{0.5}Co_{0.8}Fe_{0.2}O_{2+\delta}$ and $PrBaCo_2O_{5+\delta}$, Adv. Funct. Mater., 2018, 28, 1804355.

[161] P.E. Pearce, C. Yang, A. Iadecola, J. Rodriguez-Carvajal, G. Rousse, R. Dedryvère, A.M. Abakumov, D. Giaume, M. Deschamps, J.-M. Tarascon, A. Grimaud, Revealing the Reactivity of the Iridium Trioxide Intermediate for the Oxygen Evolution Reaction in Acidic Media, Chem. Mater., 2019, 31, 5845-5855.

[162] W. Zhang, Z. Wang, X.M. Chen, Crystal Structure Evolution and Local Symmetry of Perovskite Solid Solution $Ba[(Fe_{1/2}Nb_{1/2})_{1-X}Ti_X]O_3$ Investigated by Raman Spectra, J. Appl. Phys., 2011, 110, 064113.

[163] T.H. Shen, L. Spillane, J. Peng, Y. Shao-Horn, V. Tileli, Switchable Wetting of Oxygen-Evolving Oxide Catalysts, Nat. Catal., 2022, 5, 30-36.

[164] N. Govindarajan, A. Xu, K. Chan, How Ph Affects Electrochemical Processes, Science, 2022, 375, 379-380.

[165] T. Nishimoto, T. Shinagawa, T. Naito, K. Takanabe, Microkinetic Assessment of Electrocatalytic Oxygen Evolution Reaction over Iridium Oxide in Unbuffered Conditions, J. Catal., 2020, 391, 435-445.

[166] L. Giordano, B. Han, M. Risch, W.T. Hong, R.R. Rao, K.A. Stoerzinger, Y. Shao-Horn, Ph Dependence of Oer Activity of Oxides: Current and Future Perspectives, Catal. Today, 2016, 262, 2-10.

[167] B.-J. Kim, E. Fabbri, M. Borlaf, D.F. Abbott, I.E. Castelli, M. Nachtegaal, T.

Graule, T.J. Schmidt, Oxygen Evolution Reaction Activity and Underlying Mechanism of Perovskite Electrocatalysts at Different Ph, Mater. Adv., 2021, 2, 345-355.

[168] C. Yang, M. Batuk, Q. Jacquet, G. Rousse, W. Yin, L. Zhang, J. Hadermann, A.M. Abakumov, G. Cibin, A. Chadwick, J.-M. Tarascon, A. Grimaud, Revealing Ph-Dependent Activities and Surface Instabilities for Ni-Based Electrocatalysts During the Oxygen Evolution Reaction, ACS Energy Lett., 2018, 3, 2884-2890.

[169] S. Anantharaj, S. Kundu, S. Noda, "The Fe Effect": A Review Unveiling the Critical Roles of Fe in Enhancing Oer Activity of Ni and Co Based Catalysts, Nano Energy, 2021, 80.

[170] L. Trotochaud, S.L. Young, J.K. Ranney, S.W. Boettcher, Nickel–Iron Oxyhydroxide Oxygen-Evolution Electrocatalysts: The Role of Intentional and Incidental Iron Incorporation, J. Am. Chem. Soc., 2014, 136, 6744-6753.

[171] D. Friebel, M.W. Louie, M. Bajdich, K.E. Sanwald, Y. Cai, A.M. Wise, M.-J. Cheng, D. Sokaras, T.-C. Weng, R. Alonso-Mori, R.C. Davis, J.R. Bargar, J.K. Norskov, A. Nilsson, A.T. Bell, Identification of Highly Active Fe Sites in (Ni,Fe)OOH for Electrocatalytic Water Splitting, J. Am. Chem. Soc., 2015, 137, 1305-1313.

[172] S. Klaus, Y. Cai, M.W. Louie, L. Trotochaud, A.T. Bell, Effects of Fe Electrolyte Impurities on $Ni(OH)_2$/NiOOH Structure and Oxygen Evolution Activity, J. Phys. Chem. C, 2015, 119, 7243-7254.

[173] D.Y. Chung, P.P. Lopes, P. Farinazzo Bergamo Dias Martins, H. He, T. Kawaguchi, P. Zapol, H. You, D. Tripkovic, D. Strmcnik, Y. Zhu, S. Seifert, S. Lee, V.R. Stamenkovic, N.M. Markovic, Dynamic Stability of Active Sites in Hydr(oxy)oxides for the Oxygen Evolution Reaction, Nat. Energy, 2020, 5, 222-230.

[174] P.P. Lopes, D.Y. Chung, X. Rui, H. Zheng, H. He, P. Farinazzo Bergamo Dias Martins, D. Strmcnik, V.R. Stamenkovic, P. Zapol, J.F. Mitchell, R.F. Klie, N.M. Markovic, Dynamically Stable Active Sites from Surface Evolution of Perovskite Materials During the Oxygen Evolution Reaction, J. Am. Chem. Soc., 2021, 143, 2741-2750.

[175] H. Li, Y. Chen, J. Ge, X. Liu, A.C. Fisher, M.P. Sherburne, J.W. Ager, Z.J. Xu, Active Phase on $SrCo_{1-X}Fe_xO_{3-\delta}$ ($0 \leq X \leq 0.5$) Perovskite for Water Oxidation:

Reconstructed Surface Versus Remaining Bulk, JACS Au, 2021, 1, 108-115.

[176] L. Zhuang, Z. Li, M. Li, H. Tao, X. Mao, C. Lian, L. Ge, A. Du, Z. Xu, Z. Shao, Z. Zhu, A New Operando Surface Restructuring Pathway Via Ion-Pairing of Catalyst and Electrolyte for Water Oxidation, Chem. Eng. J., 2023, 454, 140071.

[177] T.H. Shen, L. Spillane, J. Vavra, T.H.M. Pham, J. Peng, Y. Shao-Horn, V. Tileli, Oxygen Evolution Reaction in $Ba_{0.5}Sr_{0.5}Co_{0.8}Fe_{0.2}O_{3-\delta}$ Aided by Intrinsic Co/Fe Spinel-Like Surface, J. Am. Chem. Soc., 2020, 142, 15876-15883.

[178] J.I. Jung, H.Y. Jeong, M.G. Kim, G. Nam, J. Park, J. Cho, Fabrication of $Ba_{0.5}Sr_{0.5}Co_{0.8}Fe_{0.2}O_{3-\delta}$ Catalysts with Enhanced Electrochemical Performance by Removing an Inherent Heterogeneous Surface Film Layer, Adv. Mater., 2015, 27, 266-271.

[179] Y. Inoue, Y. Miyahara, K. Miyazaki, Y. Kondo, Y. Yokoyama, T. Abe, Influence of Chemical Operation on the Electrocatalytic Activity of $Ba_{0.5}Sr_{0.5}Co_{0.8}Fe_{0.2}O_{3-\delta}$ for the Oxygen Evolution Reaction, J. Electrochem. Soc., 2022, 169, 010518.

[180] X. Cheng, B.J. Kim, E. Fabbri, T.J. Schmidt, Co/Fe Oxyhydroxides Supported on Perovskite Oxides as Oxygen Evolution Reaction Catalyst Systems, ACS Appl Mater Interfaces, 2019, 11, 34787-34795.

[181] J. Wang, H. Xie, Y. Wang, R. Ouyang, Distilling Accurate Descriptors from Multi-Source Experimental Data for Discovering Highly Active Perovskite Oer Catalysts, J. Am. Chem. Soc., 2023, 145, 11457-11465.

[182] Y. Li, R. Zhu, Y. Wang, L. Feng, Y. Liu, Center-Environment Deep Transfer Machine Learning across Crystal Structures: From Spinel Oxides to Perovskite Oxides, npj Comput. Mater., 2023, 9, 109.

[183] X. Zhu, J. Huang, M. Eikerling, Ph Effects in a Model Electrocatalytic Reaction Disentangled, JACS Au, 2023, 3, 1052-1064.

[184] J. Huang, Y. Chen, Combining Theory and Experiment in Advancing Fundamental Electrocatalysis, Curr. Opin. Electrochem., 2019, 14, A4-A9.

[185] R. Jinnouchi, F. Karsai, G. Kresse, On-the-Fly Machine Learning Force Field Generation: Application to Melting Points, Physical Review B, 2019, 100, 014105.

[186] S.H. Chang, N. Danilovic, K.-C. Chang, R. Subbaraman, A.P. Paulikas, D.D.

Fong, M.J. Highland, P.M. Baldo, V.R. Stamenkovic, J.W. Freeland, J.A. Eastman, N.M. Markovic, Functional Links between Stability and Reactivity of Strontium Ruthenate Single Crystals During Oxygen Evolution, Nat. Commun., 2014, 5, 4191.

[187] N. Danilovic, R. Subbaraman, K.-C. Chang, S.H. Chang, Y.J. Kang, J. Snyder, A.P. Paulikas, D. Strmcnik, Y.-T. Kim, D. Myers, V.R. Stamenkovic, N.M. Markovic, Activity–Stability Trends for the Oxygen Evolution Reaction on Monometallic Oxides in Acidic Environments, J. Phys. Chem. Lett., 2014, 5, 2474-2478.